Functionalized 2′-Amino-α-L-LNA - Directed Positioning of Intercalators for DNA Targeting

T. Santhosh Kumar,[†] Andreas S. Madsen,[†] Michael E. Østergaard,[‡] Sujay P. Sau,[‡] Jesper Wengel[†] and Patrick J. Hrdlicka[‡,*]

[†]Nucleic Acid Center,[‖] Department of Physics and Chemistry, University of Southern Denmark, DK-5230 Odense M, Denmark, [‡]Department of Chemistry, University of Idaho, Moscow, ID 83843-2343, USA.

SUPPORTING INFORMATION

General Experimental Section. All reagents and solvents were of analytical grade and obtained from commercial suppliers and used without further purification except for CH_2Cl_2, which was distilled prior to use. Petroleum ether of the distillation range 60-80 °C was used. Anhydrous DMF and pyridine were used as obtained from commercial suppliers. Acetonitrile was dried through storage over activated 3Å molecular sieves. Anhydrous dichloromethane, 1,2-dichloroethane, *N*,*N*′-diisopropylethylamine, THF and triethylamine were dried through storage over activated 4Å molecular sieves. Water content of the anhydrous solvents was checked by Karl-Fischer apparatus. Reactions were conducted under an atmosphere of argon whenever anhydrous solvents were used. All reactions were monitored by thin-layer chromatography (TLC) using silica gel coated plates with fluorescence indicator (SiO_2-60, F-254) which were visualized a) under UV light, b) by dipping in 5% conc. sulphuric acid in absolute ethanol (v/v) followed by heating or c) by dipping in a solution of molybdato-phosphoric acid (12.5 g/L) and cerium(IV)sulphate (5 g/L) in 3% conc. sulphuric acid in water (v/v) followed by heating. Silica gel column chromatography was performed with Silica gel 60 (particle size 0.040–0.063 mm, Merck) using moderate pressure (pressure ball). Silica gel columns were generally built with an initial starting eluent containing 1% (v/v) of Et_3N or pyridine. Evaporation of solvents was carried out under reduced pressure at a temperature not exceeding 50 °C. After column chromatography, appropriate fractions were pooled, evaporated and dried at high vacuum for at least 12 h to give obtained products in high purity (>95%), unless stated otherwise. ^{1}H NMR, ^{13}C NMR and/or ^{31}P NMR ascertained sample purity. No corrections in yields were made for solvent of crystallization. ^{1}H NMR, ^{13}C NMR and ^{31}P NMR spectra were recorded at 300 MHz, 75.5 MHz and 121.5 MHz, respectively. Chemical shifts are reported in parts per million (ppm) relative to tetramethylsilane or deuterated solvent as the internal standard (δ_H: DMSO-d_6 2.50 ppm; δ_C: DMSO-d_6 39.43 ppm). Exchangeable (ex) protons were detected by disappearance of peaks on D_2O addition. Assignments of NMR spectra are based on 2D spectra (HETCOR, COSY) and follow standard carbohydrate/nucleoside nomenclature. The carbon atom of C4′ substituents is numbered C-5″ in nucleoside derivatives.

Similar conventions apply for the corresponding hydrogen atoms. Quaternary carbons were not assigned in ^{13}C NMR. Traces of solvents in NMR spectra were identified by reference to published data.[S1] MALDI-HRMS were recorded in positive ion mode on a Fourier transform mass spectrometer. Elemental analyses were obtained from the Microanalytical Department, University of Copenhagen.

(1*S*,3*R*,4*S*,7*R*)-5-Acetyl-1-(4,4′-dimethoxytrityloxymethyl)-7-hydroxy-3-(thymin-1-yl)-2-oxa-5-azabicyclo[2.2.1]heptane 2V. Amino alcohol **1**[S2] (0.50 g, 0.87 mmol) was coevaporated with anhydrous 1,2-dichloroethane (2 × 10 mL) and dissolved in anhydrous THF (9 mL) and anhydrous Et_3N (0.5 mL, 3.59 mmol). The solution was cooled to 0 °C and Ac_2O (0.09 mL, 0.95 mmol) was added. After stirring at 0 °C for 2 h analytical TLC indicated full conversion of the starting material to desired N2′-acylated nucleoside **2V** (R_f = 0.4, 10% MeOH in CH_2Cl_2, v/v) (vide infra) and <10% of an even less polar compound (R_f = 0.6, 10% MeOH in CH_2Cl_2, v/v) presumably the corresponding N2′,O3′-diacylated species. The reaction mixture was diluted with EtOAc (25 mL), washed with brine (15 mL) and the aqueous phase back-extracted with CH_2Cl_2 (25 mL). The combined organic phase was evaporated to dryness and the resulting residue dissolved in half-saturated NH_3/MeOH (13 mL). After stirring at rt for 2 h, analytic TLC indicated that the N2′,O3′-diacylated species was converted into the desired product. The reaction mixture was evaporated to dryness and the resulting residue purified by silica gel column chromatography (0-4% MeOH in CH_2Cl_2, v/v) to afford a rotameric mixture (~1:1.6 by ^1H NMR) of nucleoside **2V** (0.47 g, 88%) as a white solid. Physical data for rotameric mixture: R_f = 0.4 (10% MeOH in CH_2Cl_2, v/v); MALDI-HRMS *m/z* 636.2376 ($[M + Na]^+$, $C_{34}H_{35}N_3O_8Na^+$ Calcd 636.2302); ^1H NMR (DMSO-d_6)[S3,S4] δ 11.49 (s, 1H, ex, NH_B), 11.26 (s, 1.6H, ex, NH_A), 7.20-7.48 (m, 36.4H, Ar_{A+B}, H-6_{A+B}), 6.87-6.96 (d, 10.4H, J = 8.4 Hz, Ar_{A+B}), 6.04-6.09 (m, 4.2H, 2.6ex, 3′-OH_{A+B}, H-1′$_A$), 6.01 (s, 1H, H-1′$_B$), 4.53 (d, 1.6H, J = 4.3 Hz, H-3′$_A$), 4.50 (s, 1.6H, H-2′$_A$), 4.48 (d, 1H, J = 4.0 Hz, H-3′$_B$), 4.41 (s, 1H, H-2′$_B$), 3.90-3.94 (d, 1.6H, J = 10.5 Hz, H-5′$_A$), 3.74 (s, 15.6H, $OCH_{3\text{-}A+B}$), 3.57-3.64 (m, 2.6H, H-5′$_A$, H-5′$_B$), 3.39-3.44

(d, 1H, J = 11.7 Hz, H-5′$_B$), 3.22-3.32 (m, 5.2H, H-5″$_{A+B}$, partial overlap with H_2O), 1.79-1.84 (m, 12.6H, 2×CH_{3-A}, CH_{3-B}), 1.71 (s, 3H, CH_{3-B}); ^{13}C NMR (DMSO-d_6) δ 169.2, 168.3, 163.8, 163.6, 158.0, 150.1, 150.0, 144.6, 135.2, 135.1, 134.4, 134.3, 129.7, 127.8, 127.6, 127.5, 126.6, 113.2 (Ar), 108.2, 107.9, 88.9, 88.5, 85.8, 85.5, 85.28, 85.24, 72.4 (C-3′$_{A/B}$), 71.2 (C-3′$_{A/B}$), 64.0 (C-2′$_B$), 60.3 (C2′$_A$, C-5″$_{A/B}$), 59.8 (C-5″$_{A/B}$), 54.9 (CH_3O), 52.7, 51.4, 21.1 (CH_3CO), 20.6 (CH_3CO), 12.3 (CH_3), 12.0 (CH_3); Anal. Calc. for $C_{34}H_{35}N_3O_8$·1/16 H_2O: C, 66.42; H, 5.76; N, 6.83; Found: C, 66.02; H, 5.88; N, 6.72.

(1*S*,3*R*,4*S*,7*R*)-1-(4,4′-Dimethoxytrityloxymethyl)-7-hydroxy-5-(pyren-1-yl)methyl-3-(thymin-1-yl)-2-oxa-5-azabicyclo[2.2.1]heptane 2W. Amino alcohol **1**[S2] (275 mg, 0.48 mmol) was dried by coevaporation with anhydrous 1,2-dichloroethane (2 × 5 mL) and redissolved in anhydrous 1,2-dichloroethane (5 mL). To this was added 1-pyrenecarbaldehyde (117 mg, 0.51 mmol) and sodium triacetoxyborohydride (153 mg, 0.72 mmol). After stirring at rt for 6 h, sat. aq. $NaHCO_3$ (2 mL) was added and the mixture diluted with EtOAc (20 mL). The organic phase was washed with sat. aq. $NaHCO_3$ (10 mL) and the aqueous phase back extracted with EtOAc (20 mL). The combined organic phase was evaporated to dryness under reduced pressure and the resulting residue was purified by silica gel column chromatography (0-65% EtOAc in petroleum ether, v/v) to afford nucleoside **2W**[S5] (252 mg, 67%) as a white solid material. R_f = 0.5 (80% EtOAc in petroleum ether, v/v); MALDI-HRMS *m/z* 810.3153 ([M + Na]$^+$, $C_{49}H_{45}N_3O_7$·Na$^+$ Calc. 810.3150); ^{1}H NMR (DMSO-d_6)[S3] δ 11.15 (s, 1H, ex, NH), 7.87-8.29 (m, 9H, Ar), 6.84-7.42 (m, 14H, H-6, Ar), 6.06 (d, 1H, ex, J = 3.7 Hz, 3′-OH), 5.92 (d, 1H, J = 1.8 Hz, H-1′), 4.72-4.81 (d, 1H, J = 13.0 Hz, CH_2Ar), 4.53 (d, 1H, J = 13.0 Hz, CH_2Ar), 4.48 (d, 1H, J = 3.7 Hz, H-3′), 3.72 (s, 6H, CH_3O), 3.49 (br s, 1H, H-2′), 3.19-3.24 (d, 1H, J = 10.3 Hz, H-5′/H-5″), 3.04-3.09 (d, 1H, J = 10.3 Hz, H-5′/H-5″), 1.54 (s, 3H, CH_3), two H-5′/H-5″ protons not visible due to signal overlap with H_2O; Selected signals ^{1}H NMR (DMSO-d_6 + 1 drop D_2O) δ 3.29-3.34 (d, 1H, J = 10.6 Hz, H-5′), 3.25-3.29 (d, 1H, J = 10.6 Hz, H-5′), 3.15-3.19 (d, 1H, J = 10.3 Hz, H-5″), 3.02-3.08 (d, 1H, J = 10.3 Hz, H-5″); ^{13}C NMR (DMSO-d_6) δ 163.8,

158.0, 150.1, 144.7, 136.6 (Ar), 135.4, 135.3, 133.4, 130.6 (Ar), 130.2 (Ar), 130.1 (Ar), 129.6 (Ar), 128.7 (Ar), 127.8 (Ar), 127.6 (Ar), 127.3 (Ar), 126.8 (Ar), 126.6 (Ar), 126.0 (Ar), 125.0 (Ar), 124.9 (Ar), 124.2 (Ar), 124.0 (Ar), 123.7 (Ar), 123.6 (Ar), 113.1 (Ar), 106.9, 90.4, 85.3, 85.1, 75.0 (C-3′), 65.6 (C-2′), 60.9 (C-5′), 58.9 (C-5″), 58.3 (CH_2Ar), 54.9 (CH_3O), 12.2 (CH_3).

(1*S*,3*R*,4*S*,7*R*)-1-(4,4′-Dimethoxytrityloxymethyl)-7-hydroxy-5-[2-(pyren-1-yl)acetyl]-3-(thymin-1-yl)-2-oxa-5-azabicyclo[2.2.1]heptane 2Y. Amino alcohol **1**[S2] (0.30 g, 0.52 mmol) was coevaporated with anhydrous 1,2-dichloroethane (2 × 5 mL) and dissolved in anhydrous CH_2Cl_2 (11 mL). To this mixture were added 1-ethyl-[3-dimethylaminopropyl]carbodiimide hydrochloride (EDC·HCl, 121 mg, 0.63 mmol) and 1-pyrenylacetic acid (163 mg, 0.63 mmol). The reaction mixture was stirred for 7 h whereupon it was diluted with CH_2Cl_2 (30 mL) and sequentially washed with brine (2 × 25 mL) and distilled water (25 mL. The organic phase was evaporated to dryness and the resulting residue purified by silica gel column chromatography (0-3% MeOH in $CHCl_3$, v/v) to afford a rotameric mixture (~1:2.5 by ^{1}H NMR) of nucleoside **2Y**[S6,S7] (0.37 g, 86%) as a white solid material. R_f = 0.6 (10% MeOH in CH_2Cl_2, v/v); MALDI-HRMS *m/z* 836.2942 ($[M+Na]^+$, $C_{50}H_{43}N_3O_8{\cdot}Na^+$ Calcd 836.2972); Selected signals ^{1}H NMR (DMSO-d_6)[S4] δ 11.65 (s, 1H, ex, NH_B), 11.29 (s, 2.5H, ex, NH_A), 6.89-8.32 (m, 80H, Ar), 6.22 (d, 1H, ex, J = 4.3 Hz, 3′-OH_B), 6.17 (d, 2.5H, J = 1.4 Hz, H-1′$_B$), 6.14 (d, 2.5H, ex, J = 4.3 Hz, 3′-OH_A), 6.08 (d, 2.5H, J = 1.4 Hz, H1′$_A$), 4.89 (s, 1H, H2′$_B$), 4.64 (s, 2.5H, H-2′$_A$), 4.61 (d, 1H, J = 4.3 Hz, H-3′$_B$), 4.55 (d, 2.5H, J = 4.3 Hz, H-3′$_A$), 1.96 (d, 7.5H, J = 1.1 Hz, $CH_{3\text{-}A}$), 1.88 (d, J = 3 Hz, $CH_{3\text{-}B}$); ^{13}C NMR (DMSO-d_6) δ 169.6, 169.2, 163.8, 163.7, 158.0, 150.4, 149.9, 144.7, 135.2, 135.1, 134.7, 134.4, 130.2, 130.1, 129.8, 129.6, 129.4, 129.0, 128.5, 128.3, 127.8, 127.7, 127.6, 127.2, 127.0, 126.8, 126.6, 126.0, 125.0, 124.9, 124.8, 124.7, 124.4, 124.0, 123.9, 123.8, 123.4, 113.2, 108.7, 108.2, 89.1, 88.5, 85.7, 85.6, 85.3, 85.2, 72.5, 71.4, 63.7, 60.8, 60.3, 60.2, 54.95, 54.93, 52.5, 51.8, 37.8, 37.6, 12.4, 11.9. This experimental description (along with ^{1}H, ^{13}C and COSY NMR spectra) has previously been published in reference S6, but is included herein for matters of completeness.

(1*S*,3*R*,4*S*,7*R*)-1-(4,4′-Dimethoxytrityloxymethyl)-7-hydroxy-5-[4-(pyren-1-yl)butanoyl]-3-(thymin-1-yl)-2-oxa-5-azabicyclo[2.2.1]heptane 2Z. Amino alcohol **1**[S2] (0.30 g, 0.52 mmol) was coevaporated with anhydrous 1,2-dichloroethane (2 × 5 mL) and dissolved in anhydrous CH_2Cl_2 (12 mL). To this were added *N*-(3-dimethylaminopropyl)-*N*′-ethylcarbodiimide hydrochloride (EDC·HCl, 120 mg, 0.63 mmol) and 4-(1-pyrenyl)butyric acid (197 mg, 0.68 mmol) at 0 °C. After warming to rt, the reaction mixture was stirred for 18 h, whereupon it was diluted with CH_2Cl_2 (30 mL) and sequentially washed with brine (25 mL) and distilled water (25 ml). The organic phase was evaporated to dryness and the resulting residue purified by silica gel column chromatography (0-2% MeOH in CH_2Cl_2, v/v) to afford a rotameric mixture (~1:1.3 by ^{1}H NMR) of **2Z** (0.28 g, 63%) as a white solid material. R_f = 0.5 (5% *i*-PrOH in CH_2Cl_2, v/v); MALDI-HRMS *m/z* 864.3279 ([M + Na]$^+$, $C_{52}H_{47}N_3O_8{\cdot}Na^+$ Calcd 864.3255); Selected signals ^{1}H NMR (DMSO-d_6)[S4] δ 6.08-6.21 (m, 4.6H, 2.3 ex, H-1′$_{A+B}$, 3′-OH$_{A+B}$), 4.63 (s, 1.3H, H-2′$_A$), 4.49-4.58 (m, 3.3H, H-2′$_B$, 2 × H-3′); Selected signals ^{1}H NMR (DMSO-d_6 + 1 drop D_2O) δ 6.08 (br s, 2.3H, H-1$_{A+B}$′), 4.63 (s, 1.3H, H-2′$_A$), 4.50-4.55 (m, 3.3H, H-2′$_B$, 2 × H-3′); ^{13}C NMR (DMSO-d_6) δ 171.5, 170.8, 163.8, 163.7, 158.0, 150.4, 150.1, 144.7, 136.6, 136.4, 135.2, 135.1, 134.5, 134.4, 130.8, 130.3, 129.8, 129.2, 128.02, 127.97, 127.8, 127.7, 127.6, 127.4, 127.3, 127.20, 127.16, 126.7, 126.4, 126.0, 124.9, 124.8, 124.7, 124.1, 124.0, 123.4, 113.2, 108.4, 107.9, 89.0, 88.4, 85.72, 85.66, 85.33, 85.29, 72.5, 72.2, 71.2, 63.3, 60.5, 60.4, 60.2, 59.8, 55.0, 52.2, 51.7, 32.5, 32.3, 26.6, 26.5, 12.4, 11.9. A trace impurity of $CHCl_3$ was identified. The compound was used in the next step without further purification.

(1*S*,3*R*,4*S*,7*R*)-5-Acetyl-7-[2-cyanoethoxy(diisopropylamino)phosphinoxy]-1-(4,4′-dimethoxytrityloxymethyl)-3-(thymin-1-yl)-2-oxa-5-azabicyclo[2.2.1]heptane 3V. Nucleoside **2V** (0.43 g, 0.70 mmol) was coevaporated with anhydrous 1,2-dichloroethane (2 × 8 mL) and dissolved in a mixture of anhydrous EtN(*i*-Pr)$_2$ in CH_2Cl_2 (5 mL, 20%, v/v). To this was added 2-cyanoethyl *N*,*N*′-(diisopropyl)phosphoramidochloridite (0.28 mL, 1.26 mmol) and after stirring the reaction mixture at rt for 1 h it was diluted with CH_2Cl_2 (20 mL), washed with sat. aq. $NaHCO_3$ (10

mL) and the aqueous phase back-extracted with CH_2Cl_2 (25 mL). The combined organic phase was evaporated to dryness and the resulting residue purified by silica gel column chromatography (0-50% acetone in petroleum ether, v/v) to afford amidite **3V** (0.51 g, 90%) as a white solid material. R_f = 0.5 (EtOAc); MALDI-HRMS *m/z* 836.3395 ($[M + Na]^+$, $C_{43}H_{52}N_5O_9PNa^+$ Calcd 836.3386); ^{31}P NMR (CH_3CN + DMSO-d_6) δ 150.6, 150.2, 150.0, 148.8.

(1*S*,3*R*,4*S*,7*R*)-7-[2-Cyanoethoxy(diisopropylamino)phosphinoxy]-1-(4,4′-dimethoxytrityloxymethyl)-5-(pyren-1-yl)methyl-3-(thymin-1-yl)-2-oxa-5-azabicyclo[2.2.1]heptane 3W. Nucleoside **2W**[S5] (0.235 g, 0.28 mmol) was coevaporated with anhydrous CH_3CN (2 × 5 mL) and suspended in anhydrous CH_2Cl_2 (1.9 mL). To this was added anhydrous *N*,*N*′-diisopropylethylamine (0.5 mL, 2.87 mmol) and 2-cyanoethyl *N*,*N*′-(diisopropyl)phosphoramidochloridite (0.14 mL, 0.63 mmol) and the reaction mixture was stirred at rt for 4 h, whereupon abs. EtOH (1 mL) was added. The mixture was diluted with CH_2Cl_2 (20 mL) and was sequentially washed with sat. aq. $NaHCO_3$ (10 mL) and brine (10 mL). The combined aqueous phase was back extracted with CH_2Cl_2 (20 mL). The combined organic phase was evaporated to dryness under reduced pressure and the resulting residue purified by silica gel column chromatography (0-50% EtOAc in petroleum ether, v/v) to afford amidite **3W**[S5] (260 mg, 88%) as a white solid material. R_f = 0.6 (80% EtOAc in petroleum ether, v/v); MALDI-HRMS *m/z* 1008.4072 ($[M + Na]^+$, $C_{58}H_{60}N_5O_8P{\cdot}Na^+$ Calc. 1008.4110); ^{31}P NMR (CH_3CN + DMSO-d_6) δ 150.7, 148.0.

(1*S*,3*R*,4*S*,7*R*)-7-[2-Cyanoethoxy(diisopropylamino)phosphinoxy]-1-(4,4′-dimethoxytrityloxymethyl)-5-[4-(pyren-1-yl)acetyl]-3-(thymin-1-yl)-2-oxa-5-azabicyclo[2.2.1]heptane 3Y. Nucleoside **2Y**[S6] (0.34 g, 0.42 mmol) was coevaporated with anhydrous 1,2-dichloroethane (2 × 5 mL) and dissolved in an anhydrous mixture of EtN(*i*-Pr)$_2$ in CH_2Cl_2 (4 mL, 20%, v/v). To this was added 2-cyanoethyl *N*,*N*′-

(diisopropyl)phosphoramidochloridite (187 µL, 0.84 mmol) and the reaction mixture was stirred at rt for 4 h, whereupon it was diluted with CH_2Cl_2 (20 mL) and washed with sat. aq. $NaHCO_3$ (10 mL). The organic phase was evaporated to dryness and the resulting residue purified by silica gel column chromatography (0-35% acetone in petroleum ether, v/v) to afford phosphoramidite **3Y**[S6] (0.33 g, 76%) as a white solid material. R_f = 0.5 (50% acetone in petroleum ether, v/v); MALDI-HRMS *m/z* 1036.4021 ($[M+Na]^+$, $C_{59}H_{60}N_5O_9P{\cdot}Na^+$ Calcd 1036.4033); ^{31}P NMR (CH_3CN + D_2O) δ 150.1, 149.8, 149.5, 147.6. This experimental description (along with ^{31}P NMR spectra and HRMS-data) has previously been published in reference S6, but is included herein for matters of completeness.

(1*S*,3*R*,4*S*,7*R*)-7-[2-Cyanoethoxy(diisopropylamino)phosphinoxy]-1-(4,4′-dimethoxytrityloxymethyl)-5-[4-(pyren-1-yl)butanoyl]-3-(thymin-1-yl)-2-oxa-5-azabicyclo[2.2.1]heptane 3Z. Nucleoside **2Z** (100 mg, 0.12 mmol) was coevaporated with anhydrous 1,2-dichloroethane (2 × 5 mL) and dissolved in a mixture of anhydrous EtN(*i*-Pr)$_2$ in CH_2Cl_2 (1.2 mL, 20%, v/v). To this was added 2-cyanoethyl *N*,*N*′-(diisopropyl)phosphoramidochloridite (32 µL, 0.14 mmol) and the reaction mixture was stirred at rt for 2 h, whereupon it was diluted with CH_2Cl_2 (20 mL) and washed with sat. aq. $NaHCO_3$ (10 mL). The organic phase was evaporated to dryness and the resulting residue purified by silica gel column chromatography (0-35% acetone in petroleum ether, v/v) to afford phosphoramidite **3Z** (45 mg, 36%) as a white solid material. R_f = 0.7 (5% MeOH in CH_2Cl_2, v/v); MALDI-MS *m/z* 1064 ($[M + Na]^+$, $C_{61}H_{64}N_5O_9P{\cdot}Na^+$ Calcd 1064); ^{31}P NMR (CH_3CN + DMSO-d_6) δ 150.5, 150.2, 149.9, 148.7.

Table S1. Representative RP-HPLC gradient protocol.[a]

Time/min	Buffer A/(v%)	Buffer B/(v%)
0	100	0
2	100	0
40	30	70
47	0	100
50	0	100
51	100	0
60	100	0

[a]Buffer A is 0.05M TEAA (triethyl ammonium acetate) pH 7.4, while buffer B is 75 % MeCN in H_2O v/v. A flow rate of 2.5 mL/min was used.

Table S2. Representative ion-exchange HPLC gradient protocol.[a]

Time/min	H_2O/(v%)	2M NaCl/(v%)	0.25M Tris-Cl/(v%)
0	88	2	10
2	88	2	10
20	55	35	10
25	10	80	10
30	10	80	10
35	88	2	10
45	88	2	10

[a] A flow rate of 1 mL/min was used.

Table S3. MALDI-MS of synthesized ONs.[a]

ON	Sequence	Found *m/z* [M-H]$^-$	Calc. *m/z* [M-H]$^-$
O1	5′-G**O**G ATA TGC	2780	2781
O2	5′-GTG A**O**A TGC	2784	2781
O3	5′-GTG ATA **O**GC	2780	2781
O4	3′-CAC **O**AT ACG	2708	2711
O5	3′-CAC TA**O** ACG	2708	2711
O6	3′-CAC **O**A**O** ACG	2738	2738
O7	5′-G**O**G A**O**A **O**GC	2839	2837
Q1	5′-G**Q**G ATA TGC	2781	2780
Q2[S2]	5′-GTG A**Q**A TGC	2783	2780
O3	5′-GTG ATA **Q**GC	2780	2780
Q4[S2]	3′-CAC **Q**AT ACG	2711	2709
Q5[S2]	3′-CAC TA**Q** ACG	2711	2709
Q6	3′-CAC **Q**A**Q** ACG	2738	2736
Q7	5′-G**Q**G A**Q**A **Q**GC	2835	2834
S1	5′-G**S**G ATA TGC	2809	2808
S2	5′-GTG A**S**A TGC	2814	2808
S3	5′-GTG ATA **S**GC	2812	2808
S4	3′-CAC **S**AT ACG	2740	2737
S5	3′-CAC TA**S** ACG	2740	2737
S6	3′-CAC **S**A**S** ACG	2789	2792
S7	5′-G**S**G A**S**A **S**GC	2916	2918
V1	5′-G**V**G ATA TGC	2822	2822
V2	5′-GTG A**V**A TGC	2820	2822
V3	5′-GTG ATA **V**GC	2820	2822
V4	3′-CAC **V**AT ACG	2749	2751
V5	3′-CAC TA**V** ACG	2754	2751
V6	3′-CAC **V**A**V** ACG	2822	2820
V7	5′-G**V**G A**V**A **V**GC	2961	2960
W1[S5]	5′-G**W**G ATA TGC	2993	2995
W2[S5]	5′-GTG A**W**A TGC	2992	2995
W3[S5]	5′-GTG ATA **W**GC	2994	2995
W4[S5]	3′-CAC **W**AT ACG	2921	2924
W5[S5]	3′-CAC TA**W** ACG	2922	2924
X1	5′-G**X**G ATA TGC	3011	3008
X2	5′-GTG A**X**A TGC	3006	3008
X3	5′-GTG ATA **X**GC	3011	3008

X4	3′-CAC **X**AT ACG	2939	2937
X5	3′-CAC TA**X** ACG	2938	2937
X6	3′-CAC **X**A**X** ACG	3193	3192
Y1	5′-G**Y**G ATA TGC	3023	3023
Y2[S7]	5′-GTG A**Y**A TGC	3023	3023
Y3	5′-GTG ATA **Y**GC	3019	3023
Y4[S6]	3′-CAC **Y**AT ACG	2952	2952
Y5[S6]	3′-CAC TA**Y** ACG	2952	2952
Y6[S6]	3′-CAC **Y**A**Y** ACG	3223	3221
Y7	5′-G**Y**G A**Y**A **Y**GC	3562	3562
Z1	5′-G**Z**G ATA TGC	3051	3051
Z2	5′-GTG A**Z**A TGC	3053	3051
Z4	3′-CAC **Z**AT ACG	2980	2980
Z5	3′-CAC TA**Z** ACG	2980	2980

[a] Monomer **O -** 2′-oxy-α-L-LNA-T; monomer **Q -** 2′-amino-α-L-LNA-T; monomer **S** - 2′-*N*-ethyl-2′-amino-α-L-LNA-T; monomer **V** - 2′-*N*-acetyl-2′-amino-α-L-LNA-T; monomer **W** - 2′-*N*-(pyren-1-yl)methyl-2′-amino-α-L-LNA-T; monomer **X** - 2′-*N*-(pyren-1-yl)carbonyl-2′-amino-α-L-LNA-T; monomer **Y** - 2′-*N*-(pyren-1-yl)acetyl-2′-amino-α-L-LNA-T; monomer **Z** - 2′-*N*-[4-(pyren-1-yl)butanoyl]-2′-amino-α-L-LNA-T; For the structure of the monomers see Fig. 1.

Figure S1. Representative thermal denaturation curves of duplexes between **D1** or **Q2**-**Z2** and complementary DNA (upper) or RNA (lower) strands.

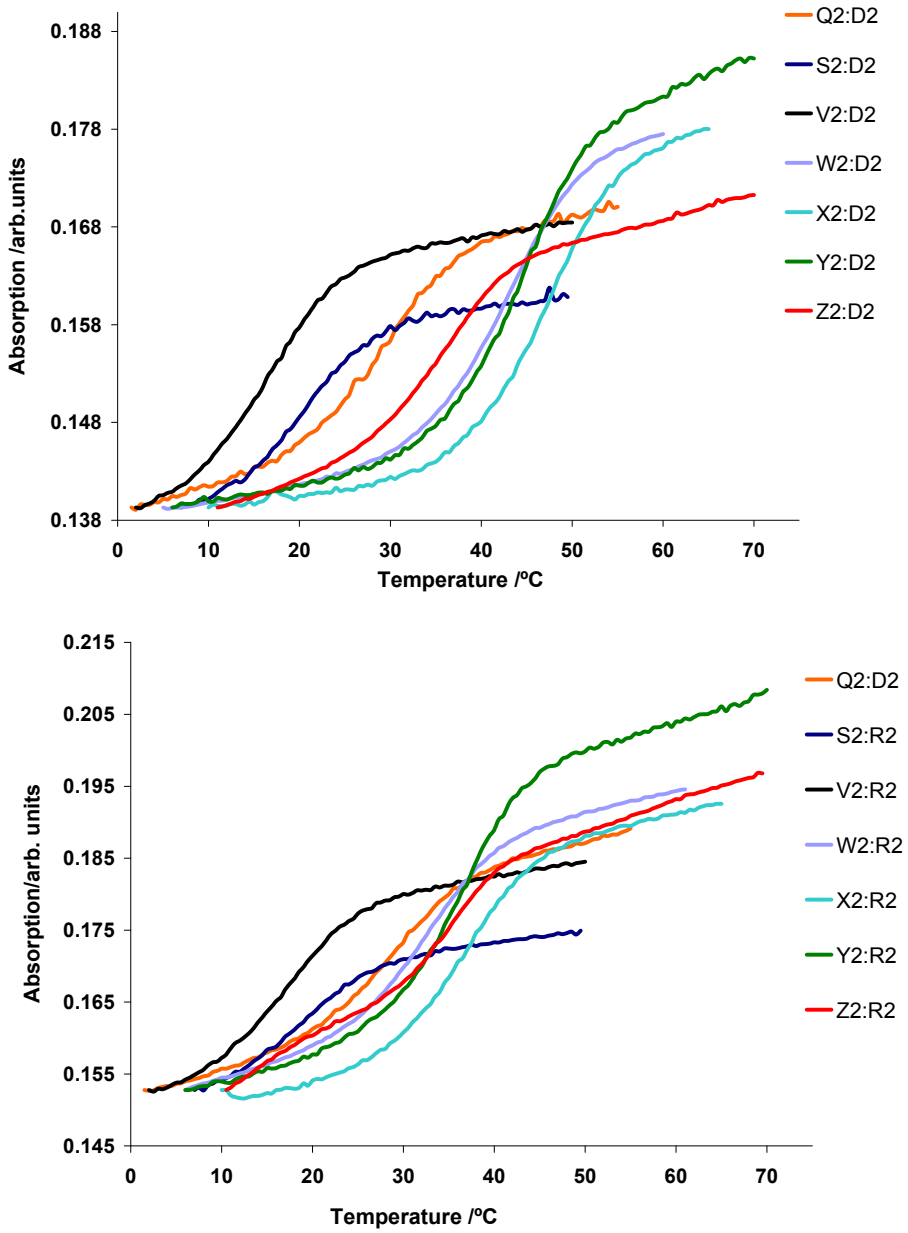

Table S4. Thermal affinity of N2′-functionalized 2′-amino-α-L-LNA and reference strands toward DNA/RNA complements at various ionic strengths.[a]

			T_m /°C		ΔT_m /°C						
ON	**Duplex**	**[Na^+] B=**	**T**	**O**	**Q**	**S**	**V**	**W**	**X**	**Y**	**Z**
B2	5′-GTG A**B**A TGC	10 mM	14.0	19.0	nd	-	-	+9.0	+13.5	+11.5	nd
D2	3′-CAC TAT ACG	110 mM	28.5	34.5	-5.5	-14.5	-18.0	+8.0	+13.0	+9.5	±0
		710 mM	36.0	41.5	nd	-13.0	-17.0	+9.0	+11.0	+9.5	nd
B2	5′-GTG A**B**A TGC	10 mM	13.0	23.0	nd	-	-	nd	+4.0	+1.5	nd
R2	3′-CAC UAU ACG	110 mM	26.5	35.0	-6.5	-16.5	-18.0	-3.0	+1.5	+1.0	-1.5
		710 mM	33.5	41.5	nd	-14.5	-17.0	nd	-1.0	-0.5	nd
D1	5′-GTG ATA TGC	10 mM	14.0	16.5	-4.5	-	-	nd	nd	+7.5	-2.5
B4	3′-CAC **B**AT ACG	110 mM	28.5	32.5	-4.5	-15.5	-20.5	+2.5	+6.5	+6.0	-3.5
		710 mM	36.0	41.5	-4.5	-14.5	-22.0	nd	nd	+4.5	-6.0
R1	5′-GUG AUA UGC	10 mM	13.0	17.5	-4.0	-	-	nd	nd	-1.5	-7.0
B4	3′-CAC **B**AT ACG	110 mM	27.5	31.0	-3.5	-11.5	-13.5	-7.5	-2.0	-0.5	-11.5
		710 mM	35.0	38.5	-2.5	-11.0	-13.5	nd	nd	-2.0	-11.0

[a] Melting temperatures (T_m values) were obtained from the maxima of the first derivatives of the melting curves (A_{260} versus temperature) recorded in high salt (HS, [Na^+] = 710 mM, [Cl^-] = 700 mM, pH 7.0 (NaH_2PO_4/Na_2HPO_4)), medium salt (MS, [Na^+] = 110 mM, [Cl^-] = 100 mM, pH 7.0 (NaH_2PO_4/Na_2HPO_4)) and low salt buffers (LS, [Na^+] = 10 mM, pH 7.0 (NaH_2PO_4/Na_2HPO_4)). In order to minimize influences from altered helical conformations on charge densities, N2′-functionalized 2′-amino-α-L-LNA were compared to α-L-LNA rather than unmodified DNA strands. ΔT_m denotes the change in T_m value relative to the corresponding duplex with an α-L-LNA strand (e.g., **W2**:**D2** relative to **O2**:**D2**). See the legend of Table 1 for additional details.

Dependence of thermal denaturation temperatures on ionic strength.

The 2-oxo-5-azabicyclo[2.2.1]heptane skeleton of α-L-amino-LNA may be partially protonated at physiological pH resulting in partial neutralization of repulsive backbone charges, in particular at low ionic strengths. Accordingly, T_m-values of duplexes between 2′-amino-α-L-LNA **Q4** and DNA/RNA complements were determined at different ionic strengths. Similar ΔT_m-values were observed for 2′-amino-α-L-LNA **Q4** relative to α-L-LNA **O4** irrespective of ionic strength suggesting that monomer **Q**, at most, is only marginally protonated at pH 7.0 (Table S4).

Compared to PyMe-α-L-amino-LNA, PyCO/PyAc/PyBu-α-L-amino-LNA exhibited larger relative increases in thermal affinity toward DNA and RNA targets at low ionic strength (Table S4). Since the 2-oxo-5-azabicyclo[2.2.1]heptanes skeletons of monomers **X**, **Y** and **Z** cannot be protonated at pH 7.0 (amide linkers), we speculate that the linker carbonyl coordinates cations rendering duplexes with increased shielding at low ionic strengths.

Discussion of sequence dependent variation of thermal denaturation temperatures.

The observed sequence dependent variation in thermal affinity of pyrene-functionalized α-L-amino-LNA **W1**-**Z5** toward DNA targets largely followed the trends of the corresponding α-L-LNA **O1**-O5 and 2′-amino-α-L-LNA **Q1**-**Q5**, although more substantial variation in T_m/mod values was noticed (Table 1). Particularly stable duplexes were formed when **W**-**Z** monomers were flanked by a 3′-purine, while comparatively less stable duplexes were observed when flanked by a 3′-pyrimidine (e.g., compare T_m/mod values for **X5**:**D1** and **X4**:**D1**). These sequence dependent variations were most pronounced for ONs with incorporations of PyMe/PyCO-α-L-amino-LNA **W**/**X** monomers. Significant sequence dependent variations have been observed for DNA duplexes modified with the closely related 2′-O-pyrenylmethyl uridine derivatives[S8] for which the pyrene moiety was suggested to intercalate and π-π overlap with the nucleobase moiety of the flanking 3′-nucleotide.[S9]

Table S5. DNA selectivity of N2′-Functionalized 2′-amino-α-L-LNA and reference strands.[a]

			ΔΔT_m/mod (DNA-RNA) /°C							
ON	**Duplex**	**B=**	**O**	**Q**	**S**	**V**	**W**	**X**	**Y**	**Z**
B1	5′-G**B**G ATA TGC		-3.5	-3.0	-1.5	-3.5	+6.5	+4.0	+4.5	+0.5
B2	5′-GTG A**B**A TGC		-2.5	-1.5	-0.5	-2.5	+9.0	+9.0	+6.0	-1.0
B3	5′-GTG ATA **B**GC		-2.5	-2.5	-4.5	-4.0	+9.0	+7.0	+5.5	-
B4	3′-CAC **B**AT ACG		-3.0	-3.5	-6.5	-9.5	+7.5	+6.0	+4.0	+5.5
B5	3′-CAC TA**B** ACG		-2.0	-2.0	-3.0	-5.5	+8.0	+8.0	+4.5	0
B6	3′-CAC **B**A**B** ACG		-1.7	-2.5	-	-	-	+5.2	+3.7	-
B7	5′-G**B**G A**B**A **B**GC		-3.3	-2.0	-	-	-	-	+4.8	-

[a] DNA selectivity defined as ΔΔT_m/mod (DNA-RNA) = ΔT_m/mod (DNA) - ΔT_m/mod (RNA). For thermal denaturation data used in these calculations see Tables 1 and 2.

Thermodynamic data of duplex formation - α-L-LNA and 2′-amino-α-L-LNA.

The markedly increased thermal affinity of α-L-LNA **O1**-**O5** toward complementary DNA, e.g., $\Delta\Delta G^{298}$ (**O2**$_{\mathbf{DNA}}$) = ΔG^{298}(**O2**:**D2**) − ΔG^{298}(**D1**:**D2**) = −5 kJ/mol is a result of a more favorable enthalpic term, i.e., ΔΔH (**O2**$_{\mathbf{DNA}}$) = ΔH(**O2**:**D2**) − ΔH(**D1**:**D2**) = −27 kJ/mol. This is largely but not completely counterbalanced by an unfavorable entropic term, i.e., $\Delta(T^{298}\Delta S)$ (**O2**$_{\mathbf{DNA}}$) = $T^{298}\Delta S$ (**O2**:**D2**) − $T^{298}\Delta S$ (**D1**:**D2**) = −22 kJ/mol (Table S6). The RNA-selectivity observed for **O1**-**O5** (Table S5), is also reflected in the thermodynamic parameters, as consistently more favorable changes in free energy are observed ($\Delta\Delta G^{298}$ (**O1-O5**$_{\mathbf{RNA}}$) = −6 to −12 kJ/mol). This stabilization results from an even more favorable enthalpic term (ΔΔH (**O1-O5**$_{\mathbf{RNA}}$) = −86 to −152 kJ/mol) than upon hybridization with DNA targets, which partially is counterbalanced by a much more unfavorable entropic contribution ($\Delta(T^{298}\Delta S)$ (**O1**-**O5**$_{\mathbf{RNA}}$) = −78 to −140 kJ/mol). These results suggests that the increase in thermal affinity of α-L-LNA **O1**-**O5** toward DNA/RNA complements is not due to preorganization of the single stranded probe, but rather the result of a more favorable stacking/hydrogen bonding geometry and/or duplex solvation.

The decreased thermal affinity of 2′-amino-α-L-LNA **Q1**-**Q5** toward DNA/RNA complements relative to α-L-LNA **O1**-**O5** (Tables 1 and 2), representing a very conservative formal exchange

from an oxy-methylene bridge to an aza-methylene bridge, is also reflected in less favorable free energy change ($\Delta\Delta G^{298}$ (**Q1**-$\mathbf{Q5_{DNA/RNA}}$) = −4 to +2 kJ/mol, Table S6). The enthalpic/entropic contributions upon hybridization of **Q1**-**Q5** with DNA complements are sequence dependent and could not be assigned to a clear pattern. Favorable enthalpic and unfavorable entropic contributions were observed for **Q1**-**Q5** upon hybridization with RNA targets as for α-L-LNA **O1**-**O5**, although the individual contributions were less pronounced. This suggests that the molecular basis for the observed trends in thermal affinity toward DNA/RNA complements is similar for the two monomers, in particular since virtually identical circular dichroism (CD) spectra and modeling structures were observed (Figs. S2, S4 and S5). Accordingly, altered solvation patterns may account for the diverging energetics of these closely related monomers.

Thermodynamic data of duplex formation – Et/Ac-α-L-amino-LNA.

The extraordinarily decreased stabilities of duplexes between Et-α-L-amino-LNA and DNA/RNA complements ($\Delta\Delta G^{298}$ (**S1**-$\mathbf{S5_{DNA/RNA}}$) = +5 to +8 kJ/mol), largely resulted from very unfavorable entropic components, which were particularly noticeable with complementary RNA ($\Delta(T^{298}\Delta S)$ (**S1**-$\mathbf{S5_{RNA}}$) = −80 to −101 kJ/mol), and only partially offset by very advantageous enthalpic components ($\Delta\Delta H$ (**S1**-$\mathbf{S5_{RNA}}$) = −74 to −94 kJ/mol, Table S6). Duplexes between the even more destabilizing Ac-α-L-amino-LNA ($\Delta\Delta G^{298}$ (**V1**-$\mathbf{V5_{DNA/RNA}}$) = +6 to +12 kJ/mol) and RNA targets, generally exhibited similar trends in enthalpy/entropy contributions as Et-α-L-amino-LNA **S1**-**S5**. The individual enthalpy/entropy contributions were, however, much smaller in magnitude, i.e., $\Delta\Delta H$ (**V1**-$\mathbf{V5_{RNA}}$) = −14 to −89 kJ/mol and $\Delta(T^{298}\Delta S)$ (**V1**-$\mathbf{V5_{RNA}}$) = −23 to −96 kJ/mol. The collected data did not allow delineation of energetics of duplexes between Ac-α-L-amino-LNA **V1**-**V5** and DNA complements. The thermodynamic data, along with CD-spectra and molecular modeling studies (Figs. 2, S6 and S7), suggest that the unfavorable entropic contributions observed upon hybridization of Et-α-L-amino-LNA or Ac-α-L-amino-LNA with DNA/RNA complements are a result of solvation effects rather than major structural changes of the resulting duplexes.

Thermodynamic data of duplex formation - N2′-pyrene-functionalized 2′-amino-α-L-LNA.

The very pronounced stabilization of duplexes between PyMe-α-L-amino-LNA **W1**-**W5** and DNA targets ($\Delta\Delta G^{298}$ (**W1**-**W5**$_{\mathbf{DNA}}$) = −5 to −12 kJ/mol) originated from favorable entropic stabilization ($\Delta(T^{298}\Delta S)$ (**W1**-**W5**$_{\mathbf{DNA}}$) = +24 to +54 kJ/mol, Table S6) that only to some extent was counteracted by an unfavorable enthalpy component ($\Delta\Delta H$ (**W1**-**W5**$_{\mathbf{DNA}}$) = +19 to +44 kJ/mol). The generally observed stabilization of duplexes with RNA complements ($\Delta\Delta G^{298}$ (**W1**-**W5**$_{\mathbf{RNA}}$) = +3 to −6 kJ/mol) resulted from favorable enthalpic components ($\Delta\Delta H$ (**W1**-**W5**$_{\mathbf{DNA}}$) = −1 to −92 kJ/mol). However, direct comparison with the more relevant 2′-amino-α-L-LNA **Q1**-**Q5** reference strands, revealed that favorable entropic contributions play prominent roles in duplex formation with RNA targets ($\Delta(T^{298}\Delta S)$ (**W1**-**W5**$_{\mathbf{RNA}}$) = −4 to −86 kJ/mol and $\Delta(T^{298}\Delta S)$ (**Q1**-**Q5**$_{\mathbf{RNA}}$) = −24 to −94 kJ/mol, Table S6).

PyCO-α-L-amino-LNA exhibited the most dramatic stabilization of duplexes among all studied N2′-functionalized 2′-amino-α-L-LNA with DNA ($\Delta\Delta G^{298}$ (**X1**-**X5**$_{\mathbf{DNA}}$) = −10 to −22 kJ/mol) and RNA targets ($\Delta\Delta G^{298}$ (**X1**-**X5**$_{\mathbf{RNA}}$) = −8 to −12 kJ/mol). Thus, the change in linker chemistry from alkyl to amide (**W**→**X**) resulted in 4-12 kJ/mol of additional duplex stabilization. Duplex formation between PyCO-α-L-amino-LNA **X1**-**X5** and DNA/RNA complements to a larger extend was favored by more favorable enthalpic contributions than with **W1**-**W5** (e.g., $\Delta\Delta H$ (**X1**-**X5**$_{\mathbf{DNA}}$) = −8 to −61 kJ/mol, Table S6). Direct comparison of thermodynamic data with 2′-amino-α-L-LNA **Q1**-**Q5**, however, suggests that entropic factors also contribute favorably to duplex stabilization.

The very stable duplexes formed between PyAc-α-L-amino-LNA **Y1**-**Y5** and complementary DNA strands ($\Delta\Delta G^{298}$ (**Y1**-**Y5**$_{\mathbf{DNA}}$) = −9 to −14 kJ/mol) resulted from more favorable entropic contributions, which were partially balanced by unfavorable enthalpic contributions ($\Delta(T^{298}\Delta S)$ (**Y1**-**Y5**$_{\mathbf{DNA}}$) = +7 to +19 kJ/mol, and $\Delta\Delta H$ (**Y1**-**Y5**$_{\mathbf{DNA}}$) = −2 to +8 kJ/mol, Table S6). In contrast, favorable duplex formation with RNA complements ($\Delta\Delta G^{298}$ (**Y1**-**Y5**$_{\mathbf{RNA}}$) = −3 to −10 kJ/mol) resulted from favorable enthalpic contributions ($\Delta\Delta H$ (**Y1**-**Y5**$_{\mathbf{DNA}}$) = −9 to −73 kJ/mol). Direct comparison with 2′-amino-α-L-LNA **Q1**-**Q5** reveals that entropic contributions are a factor in duplex

formation ($\Delta(T^{298}\Delta S)$ (**Y1**-**Y5**$_{\mathbf{RNA}}$) = −6 to −63 kJ/mol and $\Delta(T^{298}\Delta S)$ (**Q1**-**Q5**$_{\mathbf{RNA}}$) = −24 to −94 kJ/mol, Table S6). Thus, energetics of duplex formation between PyAc-α-L-amino-LNA **Y1**-**Y5** and DNA/RNA complements resemble those of PyMe-α-L-amino-LNA **W1**-**W5** more closely than PyCO-α-L-amino-LNA **X1**-**X5**, suggesting an intricate interplay between linker length/chemistry.

Further elongation of the alkanoyl linker (**Y**→**Z**), resulted in lower duplex stability with DNA complements ($\Delta\Delta G^{298}$ (**Z1**-**Z5**$_{\mathbf{DNA}}$) = −1 to −5 kJ/mol), which originated from less favorable entropic contributions ($\Delta(T^{298}\Delta S)$ (**Z1**-**Z5**$_{\mathbf{DNA}}$) = −1 to −10 kJ/mol, Table S6). The collected data did not allow delineation of energetics for duplex formation between PyBu-α-L-amino-LNA **Z1**-**Z5** and RNA complements.

Table S6. Thermodynamic parameters derived from thermal denaturation curves using van't Hoff plots.[a]

		Complementary DNA			Complementary RNA		
		ΔG^{298} [$\Delta\Delta G^{298}$]	ΔH [$\Delta\Delta H$]	$T^{298}\Delta S$ [$\Delta(T^{298}\Delta S)$]	ΔG^{298} [$\Delta\Delta G^{298}$]	ΔH [$\Delta\Delta H$]	$T^{298}\Delta S$ [$\Delta(T^{298}\Delta S)$]
ON	**Sequence**	(kJ/mol)	(kJ/mol)	(kJ/mol)	(kJ/mol)	(kJ/mol)	(kJ/mol)
D1	5′-GTG ATA TGC	−41	−327	−286	−38	−275	−237
D2	3′-CAC TAT ACG	−41	−327	−286	−39	−271	−232
O1	5′-G**O**G ATA TGC	−43 [−2]	−375 [−48]	−332 [−46]	−45 [−7]	−372 [−97]	−327 [−90]
O2	5′-GTG A**O**A TGC	−46 [−5]	−354 [−27]	−308 [−22]	−46 [−8]	−361 [−86]	−315 [−78]
O3	5′-GTG ATA **O**GC	−45 [−4]	−377 [−50]	−332 [−46]	−45 [−7]	−376 [−101]	−331 [−94]
O4	3′-CAC **O**AT ACG	−45 [−4]	−374 [−47]	−329 [−43]	−45 [−6]	−372 [−101]	−327 [−95]
O5	3′-CAC TA**O** ACG	−47 [−6]	−352 [−25]	−305 [−19]	−51 [−12]	−423 [−152]	−372 [−140]
Q1	5′-G**Q**G ATA TGC	−42 [−1]	−344 [−17]	−302 [−16]	−42 [−4]	−344 [−69]	−302 [−65]
Q2	5′-GTG A**Q**A TGC	−41 [0]	−312 [+15]	−271 [+15]	−40 [−2]	−302 [−27]	−261 [−24]
Q3	5′-GTG ATA **Q**GC	−41 [0]	−349 [−22]	−308 [−22]	−40 [−2]	−328 [−53]	−288 [−51]
Q4	3′-CAC **Q**AT ACG	−39 [+2]	−310 [+17]	−271 [+15]	−40 [−1]	−337 [−66]	−297 [−65]
Q5	3′-CAC TA**Q** ACG	−43 [−2]	−334 [−7]	−291 [−5]	−42 [−3]	−368 [−97]	−326 [−94]
S1	5′-G**S**G ATA TGC	−33 [+8]	−339 [−12]	−306 [−20]	−32 [+6]	−349 [−74]	−317 [−80]
S2	5′-GTG A**S**A TGC	−33 [+8]	−349 [−22]	−316 [−30]	−31 [+7]	−352 [−77]	−321 [−84]
S3	5′-GTG ATA **S**GC	ND	ND	ND	−31 [+7]	−362 [−87]	−331 [−94]
S4	3′-CAC **S**AT ACG	ND	ND	ND	−32 [+7]	−365 [−94]	−333 [−101]
S5	3′-CAC TA**S** ACG	−34 [+7]	−338 [−11]	−304 [−18]	−34 [+5]	−364 [−93]	−330 [−98]
V1	5′-G**V**G ATA TGC	ND	ND	ND	−32 [+6]	−294 [−19]	−262 [−25]
V2	5′-GTG A**V**A TGC	−29 [+12]	−295 [+32]	−266 [+20]	−30 [+8]	−303 [−28]	−273 [−36]
V3	5′-GTG ATA **V**GC	ND	ND	ND	−29 [+9]	−289 [−14]	−260 [−23]
V4	3′-CAC **V**AT ACG	ND	ND	ND	−31 [+8]	−324 [−53]	−293 [−61]
V5	3′-CAC TA**V** ACG	−31 [+10]	−341 [−14]	−310 [−24]	−32 [+7]	−360 [−89]	−328 [−96]
W1	5′-G**W**G ATA TGC	−46 [−5]	−308 [+19]	−262 [+24]	−39 [−1]	−292 [−17]	−253 [−16]
W2	5′-GTG A**W**A TGC	−53 [−12]	−307 [+20]	−254 [+32]	−44 [−6]	−328 [−53]	−284 [−47]
W3	5′-GTG ATA **W**GC	−49 [−8]	−305 [+22]	−256 [+30]	−39 [−1]	−293 [−18]	−254 [−17]
W4	3′-CAC **W**AT ACG	−46 [−5]	−297 [+30]	−251 [+35]	−36 [+3]	−272 [−1]	−236 [−4]
W5	3′-CAC TA**W** ACG	−51 [−10]	−283 [+44]	−232 [+54]	−45 [−6]	−363 [−92]	−318 [−86]
X1	5′-G**X**G ATA TGC	−51 [−10]	−346 [−19]	−295 [−9]	−46 [−8]	−342 [−67]	−296 [−59]
X2	5′-GTG A**X**A TGC	−59 [−18]	−348 [−21]	−289 [−3]	−49 [−11]	−343 [−68]	−294 [−57]
X3	5′-GTG ATA **X**GC	−53 [−12]	−335 [−8]	−282 [+4]	−46 [−8]	−311 [−36]	−265 [−28]
X4	3′-CAC **X**AT ACG	−51 [−10]	−340 [−13]	−289 [−3]	ND	ND	ND
X5	3′-CAC TA**X** ACG	−63 [−22]	−388 [−61]	−325 [−39]	−51 [−12]	−379 [−108]	−328 [−96]
Y1	5′-G**Y**G ATA TGC	−50 [−9]	−319 [+8]	−269 [+17]	−44 [−6]	−302 [−27]	−258 [−21]
Y2	5′-GTG A**Y**A TGC	−54 [−13]	−321 [+6]	−267 [+19]	−48 [−10]	−333 [−58]	−285 [−48]
Y3	5′-GTG ATA **Y**GC	−51 [−10]	−321 [+6]	−270 [+16]	−44 [−6]	−298 [−23]	−254 [−17]
Y4	3′-CAC **Y**AT ACG	−50 [−9]	−329 [−2]	−279 [+7]	−42 [−3]	−280 [−9]	−238 [−6]
Y5	3′-CAC TA**Y** ACG	−55 [−14]	−322 [+5]	−267 [+19]	−49 [−10]	−344 [−73]	−295 [−63]
Z1	5′-G**Z**G ATA TGC	−42 [−1]	−338 [−11]	−296 [−10]	−40 [−2]	−299 [−24]	−259 [−22]
Z2	5′-GTG A**Z**A TGC	−46 [−5]	−336 [−9]	−290 [−4]	ND	ND	ND
Z4	3′-CAC **Z**AT ACG	−42 [−1]	−337 [−10]	−295 [−9]	ND	ND	ND
Z5	3′-CAC TA**Z** ACG	−46 [−5]	−333 [−6]	−287 [−1]	−47 [−8]	−434 [−163]	−387 [−155]

[a] Thermal denaturation curves were obtained as described in Tables 1 and 2. $\Delta\Delta G^{298}$, $\Delta\Delta H$ and $\Delta(T^{298}\Delta S)$ change in ΔG^{298}, ΔH and $\Delta(T^{298}\Delta S)$ values, respectively, calculated relative to **D1**:**D2** and **D1**:**R2** reference duplexes).

Protocol for circular dichroism studies.

Spectra were recorded on a CD spectrometer using 4.0 μM concentration of each strand in thermal denaturation buffer. Measurements were performed at 5 °C using 5 mm path length optical cells and a final volume of 1.0 mL. Prior to measurement, the duplexes were annealed. CD-spectra were recorded from 200-600 nm for duplexes containing pyrene-functionalized 2′-amino-α-L-LNA building blocks, while a range of 200-350 nm was employed for all other studied duplexes. The resulting spectra were the average of 5 scans with a scan speed of 100 nm/min.

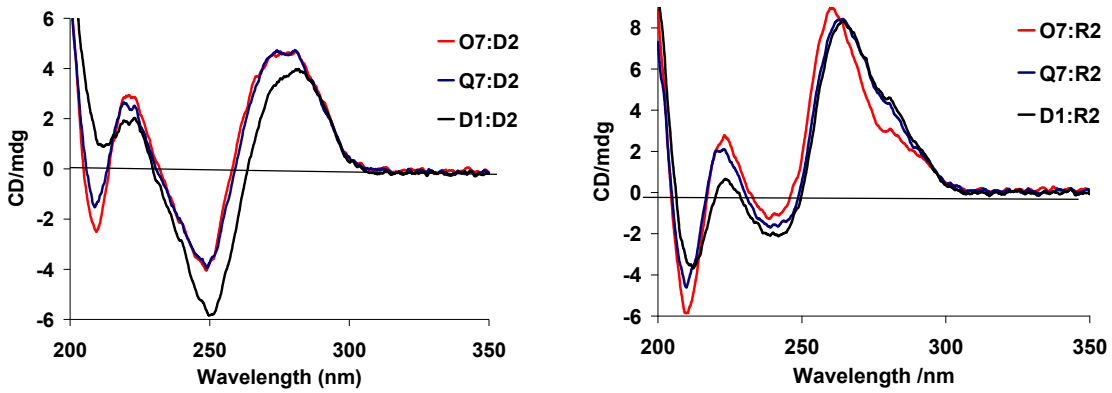

Figure S2. Circular dichroism spectra of duplexes between **O7**, **Q7** or unmodified **D1** and complementary DNA (**D2**) or RNA (**R2**). Sequence context of B7-series is 5′-G**B**G A**B**A **B**GC. For the structures of **O** and **Q** monomers see Fig. 1.

Protocol for molecular modeling studies. All modified duplexes were constructed from unmodified **D1**:**D2** duplexes (standard B-type duplex geometry) and subsequently modified in MacroModel V9.1[S10] to give the duplexes of interest. The charge of the phosphodiester backbone was neutralized with sodium ions, which were placed 3.0 Å from the two non-bridging oxygen atoms, and restrained to this distance by a force constant of 100 kJ/mol·Å^2. For all modified duplexes a preliminary minimization was conducted using the Polak-Ribiere conjugate gradient method (convergence criteria 0.1 kJ/mol·Å), the all-atom AMBER force field[S11] and GB/SA solvation model[S12] as implemented in MacroModel V9.1, having all atoms frozen, except those in the sugar moiety and the N2′-functionality of the modified monomer and the adjacent phosphodiester groups (including O3′ of the preceding nucleotide and O5′ of the following nucleotide). Non-bonded interactions were treated with extended cut-offs (van der Waals 8.0 Å and electrostatics 20.0 Å). This initial step, afforded preliminary minimized duplexes between N2′-functionalized 2′-amino-α-L-LNA and DNA complements where the N2′-functionality was positioned in the major groove. These duplex structures were subsequently subjected to a Monte Carlo conformational search, during which the torsion angles of N2′-functionalities were sampled (see below, torsion angles along bonds drawn in red were sampled). The conformational space of duplex **S2**:**D2** was sampled by variation of N2′-stereoconfiguration (*S*/*R*) and the N2′-CH_2 torsion angle (see below). The conformational space of duplex **V2**:**D2** was sampled by variation of the N2′-C(O) torsion angle. The conformational space of duplex **W2**:**D2** was sampled by variation of the N2′-stereoconfiguration (*S*/*R*) and the N2′-CH_2 and CH_2-$C1_{Py}$ torsion angles. The conformational space of duplex **X2**:**D2** was sampled by variation of the N2′-C(O) and C(O)-$C1_{Py}$ torsion angles. The conformational space of duplex **Y2**:**D2** was sampled by variation of the N2′-C(O), C(O)-CH_2 and CH_2-$C1_{Py}$ torsion angles. The conformational space of duplex **Z2**:**D2** was sampled by variation of the N2′-C(O), C(O)-$CH_{2,\alpha}$, $CH_{2,\alpha}$-$CH_{2,\beta}$, $CH_{2,\beta}$-$CH_{2,\gamma}$ and $CH_{2,\gamma}$-$C1_{Py}$ torsion angles.

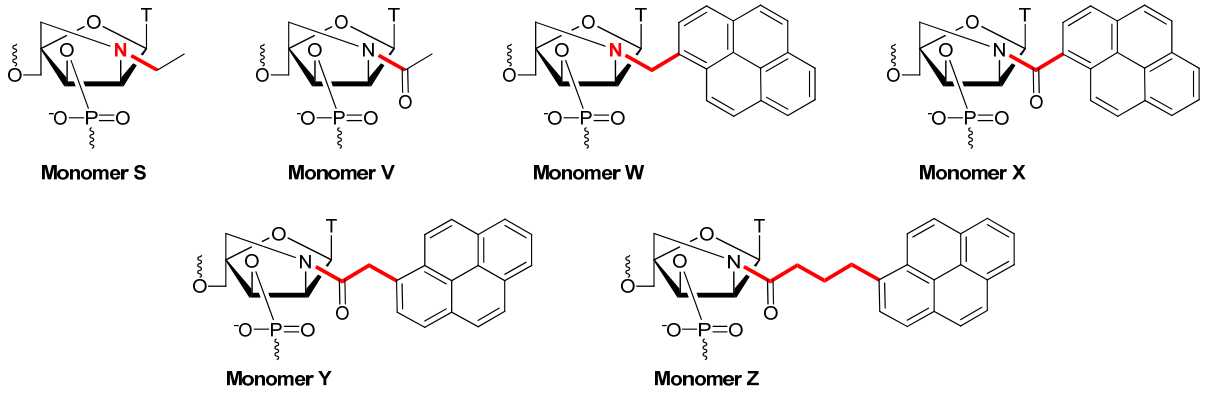

1000 structures were generated and minimized as described above allowing all atoms to move freely during while restraining the following interatomic distances: a) sodium ions were restrained as described above, b) hydrogen bonding between the **B$_5$**-moiety of the investigated duplexes and the corresponding **A$_{14}$** [(T)N3-*H*···*N1*(A), distance 2.00 Å and (T)O4···*H*-N6(A), distance 1.85 Å] as well as hydrogen bonding of the outermost base pair [(C)O2···*H*-N2(G), distance 1.98 Å, (C)*N3*···*H*-N1(G), distance 1.94 Å and (C)N4-*H*···*O*-6(G), distance 1.89 Å] was restrained by a force constant of 100 kJ/mol·Å^2. The N2′-functionalities of the most stable Monte Carlo structures for duplexes **S2**:**D2** and **V2**:**D2** pointed toward the major groove, including two structures of **V2**:**D2** of comparable energy (within 2 kJ/mol) featuring the two rotamer representations of the N2′-acetyl moiety. Accordingly, both structures of **V2**:**D2** were included as starting structures in the subsequent stochastic dynamics (SD) simulation (5 ns, simulation temperature 300 K, time step 2.2 fs, SHAKE all bonds to hydrogen) using the same restraints as during the Monte Carlo search, during which 500 structures were sampled and subsequently minimized. The most stable Monte Carlo structures for pyrene-functionalized duplexes **W2**:**D2**, **X2**:**D2** and **Y2**:**D2** featured the N2′-functionalities intercalated at the 3′-side of the **B$_5$**:**A$_{14}$** base pair and were used in SD simulations as described for **S2**:**D2** and **V2**:**D2** above. The most stable Monte Carlo structure for **Z2**:**D2** also featured the pyrene moiety of the N2′-functionality intercalated at the 3′-side of the **Z$_5$**:**A$_{14}$** base pair. However, due to the many degrees of freedom of the linker of 2′-*N*-[4-(pyren-1-yl)butanoyl]-2′-

amino-α-L-LNA monomer **Z**, several alternative low energy Monte Carlo structures were found including structures featuring a non-intercalated pyrene interacting with either the brim of the major groove or the Hoogsteen face of the nucleobases along the floor of the major groove, or even intercalation of the pyrene moiety between $\mathbf{A_6}$ and $\mathbf{T_7}$. Accordingly, dynamics simulations of **Z2**:**D2** were performed where the pyrene moiety was either intercalated or positioned in the major groove.

Additional structural discussion

The lowest energy structure of the duplex between α-L-LNA **O2** and the complementary DNA strand **D2** (Fig. S4), as expected[S13] and as observed for reference duplex **D1**:**D2** (Fig. S3), adopted a global B-type geometry, i.e., right-handed double-stranded helix with a narrow and deep minor groove and all nucleobases in *anti* conformations with well-preserved Watson-Crick base pairing. This also correlated well with the circular dichroism spectrum of **O7**:**D2**, which was very similar to the spectrum of the corresponding unmodified reference duplexes **D1**:**D2**, displaying features typical of a B-type duplex, i.e., a negative band at ~250 nm and a positive band at ~277 nm (Fig. S2).[S14] CD-spectra of **O7**:**R2** and **D1**:**R2** were very also similar, suggesting a globally intermediate A/B-type geometry, as has been reported previously.[S15] In agreement with the conformational rigidity of the α-L-LNA skeleton, the furanose ring of monomer **O** in the model structure of **O2**:**D2** displayed a pronounced *North* conformation[S16] with a pseudorotational phase angles $P = 17° \pm 5°$ compared with $P = 100° \pm 27°$ for $\mathbf{T_5}$ in **D1**:**D2**, Table S7). Furthermore, very characteristic local perturbations in the backbone of **O2**:**D2** were observed, which are needed to accommodate the inverted configurations at C2′-, C3′- and C4′-positions of α-L-LNA monomer **O**.[S13] Thus a change of γ-, δ- and ζ-torsion angles of $\mathbf{O_5}$ from the +*sc*, +*sc* and –*sc* ranges typically encountered in DNA duplexes, to *ap,* –*sc* and +*sc* ranges, respectively, was observed.[S17] Hereby, O5′, O3′ and N1, as well as the C5′-atom and the attached phosphodiester group of α-L-LNA monomer **O** superimpose onto the reference DNA strand as previously observed.[S18] Furthermore, the glycosidic torsion angle of α-L-LNA monomer **O** in **O2**:**D2** adopted a more pronounced *ap* conformation relative to $\mathbf{T_5}$ in

D1:**D2** (χ = -175° ± 8° and -143° ± 15°, respectively, Table S8), which has been suggested to be necessary for optimal Watson-Crick base pairing and base stacking of α-L-LNA thymidine monomers.[S13] These observations, in unison, provided credibility to the validity of the computational protocol.

The marked loss in thermal affinity of ONs toward DNA/RNA complements upon changing from an oxy-methylene bridge to an aza-methylene bridge (**O**→**Q**) is intriguing (Tables 1 and 2). The model structures of **O2**:**D2** and **Q2**:**D2** (Figs. S4 and S5, respectively) were virtually identical, which was further underlined by very similar circular dichroism spectra of **Q7**:**D2** and **O7**:**D2** (Fig. S2). Like α-L-LNA monomer **O**, monomer **Q** in **Q2**:**D2** exhibited a pronounced *North* conformation *P* = 15° ± 6° (Table S7), and a glycosidic torsion angle in the *ap* range (Table S8). These observations suggest that the minimally increased bulk of the 2′-amino group of monomer **Q**, does not pose a steric problem for duplex formation *per se*. In absence of desirable structural studies (X-ray structures or solution NMR studies), several hypotheses may be envisioned to rationalize the decreased thermal affinities toward DNA/RNA complements observed for 2′-amino-α-L-LNA relative to α-L-LNA:

- Incorporation of the closely related 2′-amino-DNA monomers (*ribo*-configured) into RNA strands destabilizes duplexes with RNA complements,[S19] although the structure of the duplex is not perturbed relative to a corresponding unmodified RNA duplex.[S20] This has led to the suggestion that destabilization of the RNA duplex is not a consequence of structural destabilization of the RNA duplex *per se*, but rather due to *stabilization* of the single stranded RNA strand by hydrogen bonding between the protonated 2′-amino group and a non-bridging oxygen of the 3′-phosphodiester group.[S19,S20] However, thermal denaturation temperatures obtained at different ionic strengths (Table S4) do not suggest appreciable protonation of 2′-amino-α-L-LNA.

- The decreased electronegativity of a nitrogen atom compared to an oxygen atom has been suggested to induce a slight "floppyness" in 1′,2′-azetidine-fused pyrimidines relative to their oxy-counterparts and thereby explain decreased destabilization.[S21] Similar effects could render the 2-oxa-5-azabicyclo[2.2.1]heptane skeleton of monomer **Q** slightly more "floppy" than the corresponding bicyclic skeleton of α-L-LNA. However, similar ranges of pseudorotational angles are observed for **O** and **Q** monomers in **O2**:**D2** and **Q2**:**D2** (Table S7).
- We have suggested that monomer **Q** may be in equilibrium with monomer **L**, which has been demonstrated to induce large decreases in thermal affinity toward DNA/RNA complements.[S2] However, since ^{1}H NMR studies only suggest limited amounts (if any) of monomer **L** at equilibrium, this is less likely to explain the lower thermal affinity toward DNA/RNA strands relative to α-L-LNA.

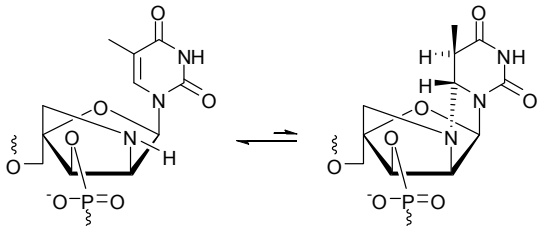

Monomer Q **Monomer L**

- Single crystal structures of B-type DNA solved to ultra-high resolution have revealed that the phosphate-backbone is stabilized by a network of structural water molecules.[S22,S23] This first shell of hydration is primarily located at the edge of the minor and major grooves, but occasionally extends above the sugar residues (toward the major groove), i.e., in positions that could be occupied by the amino group of monomer **Q** potentially leading to interference.

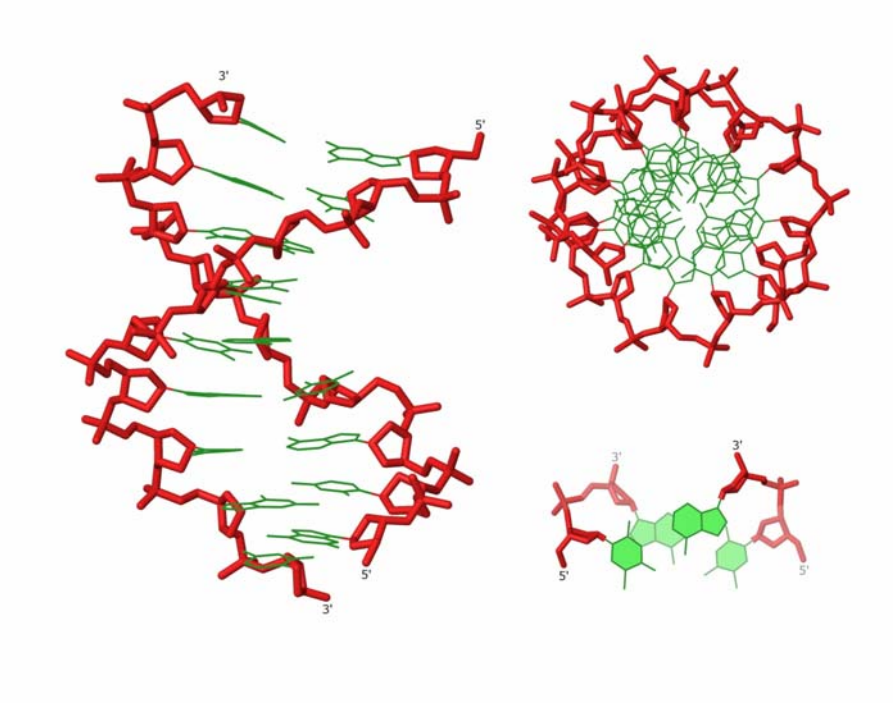

Figure S3. Three representations of the lowest energy structure of **D1**:**D2**, side view (left), top view (upper right) and enlarged view of the three central base pairs (lower right). For clarity hydrogens, sodium ions and bond orders have been omitted. Coloring scheme: nucleobases, yellow; sugar-phosphate backbone, red.

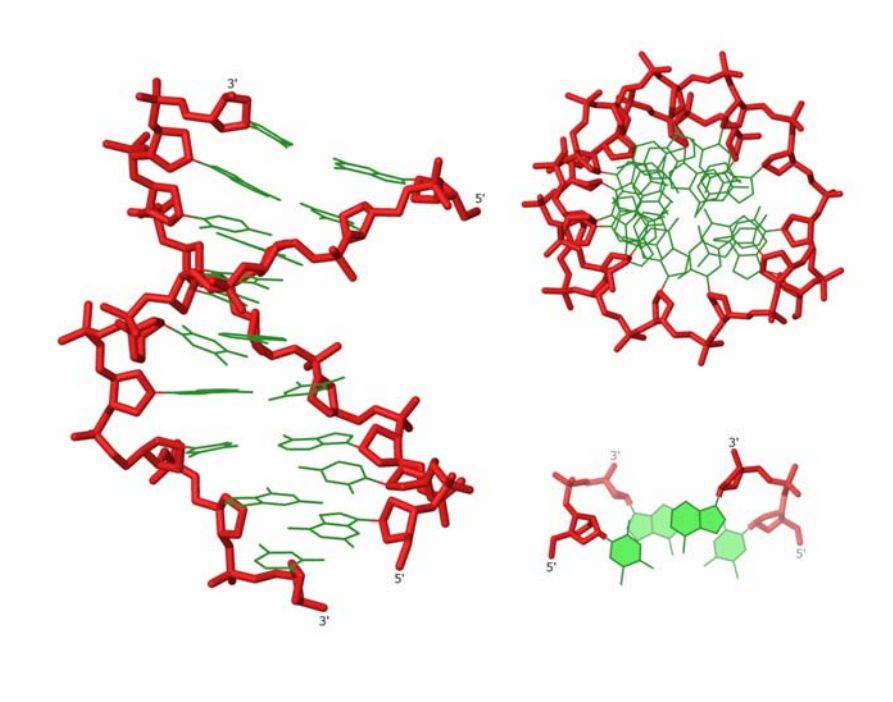

Figure S4. Three representations of the lowest energy structure of **O2**:**D2**, side view (left), top view (upper right) and enlarged view of the three central base pairs (lower right). Coloring scheme as in Fig. S3.

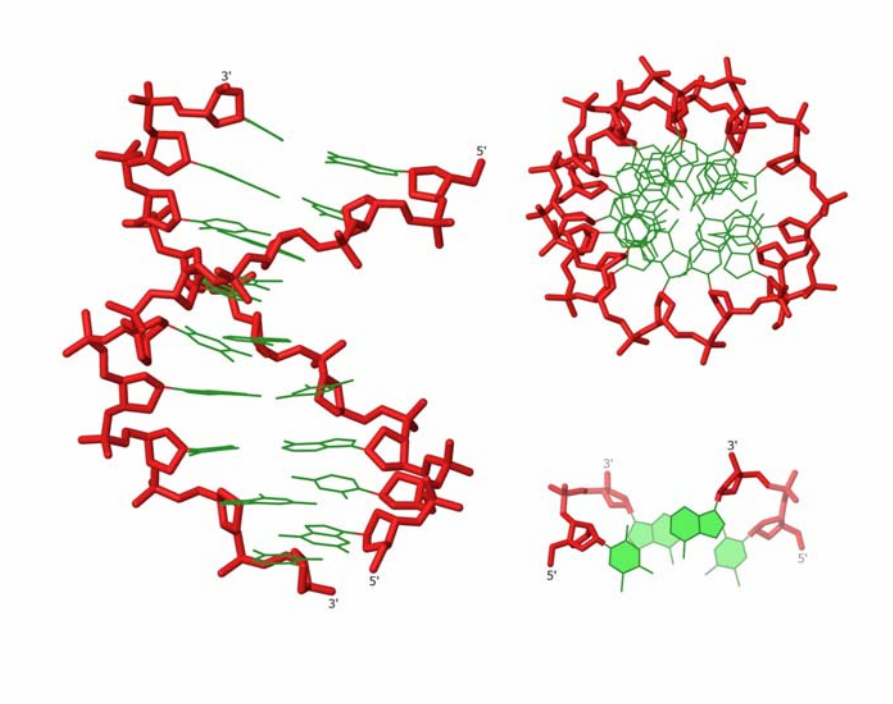

Figure S5. Three representations of the lowest energy structure of **Q2**:**D2**, side view (left), top view (upper right) and enlarged view of the three central base pairs (lower right). Coloring scheme as in Fig. S3.

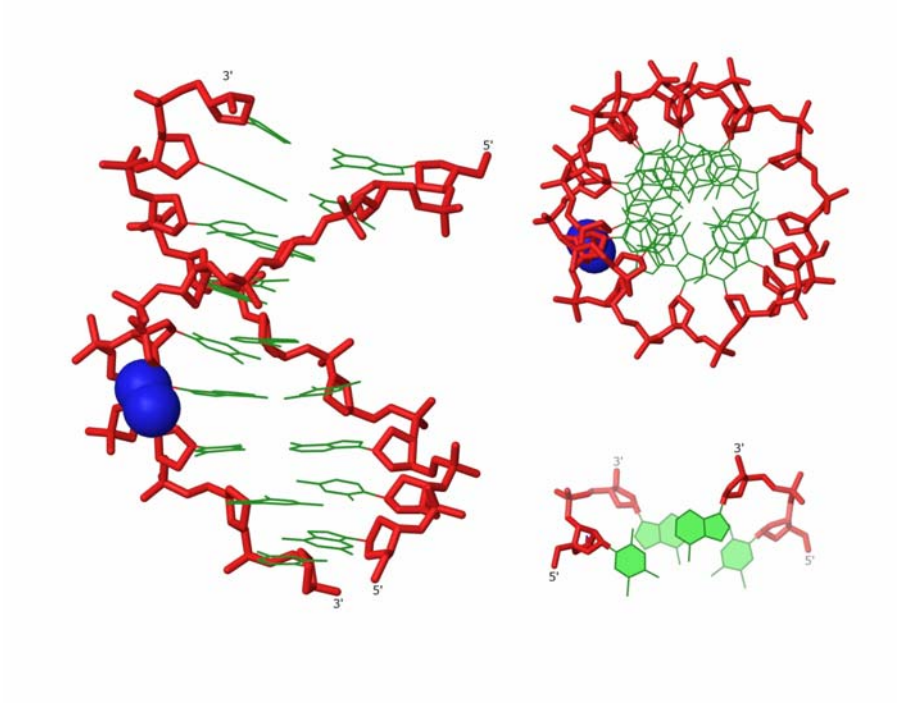

Figure S6. Three representations of the lowest energy structure of **S2**:**D2**, side view (left), top view (upper right) and truncated top view showing $\mathbf{S_5A_6}$:$\mathbf{T_{13}A_{14}}$ (lower right). For numbering of nucleotides see Fig. 4. Coloring scheme as in Fig S3 except for ethyl moiety of monomer **S**, blue.

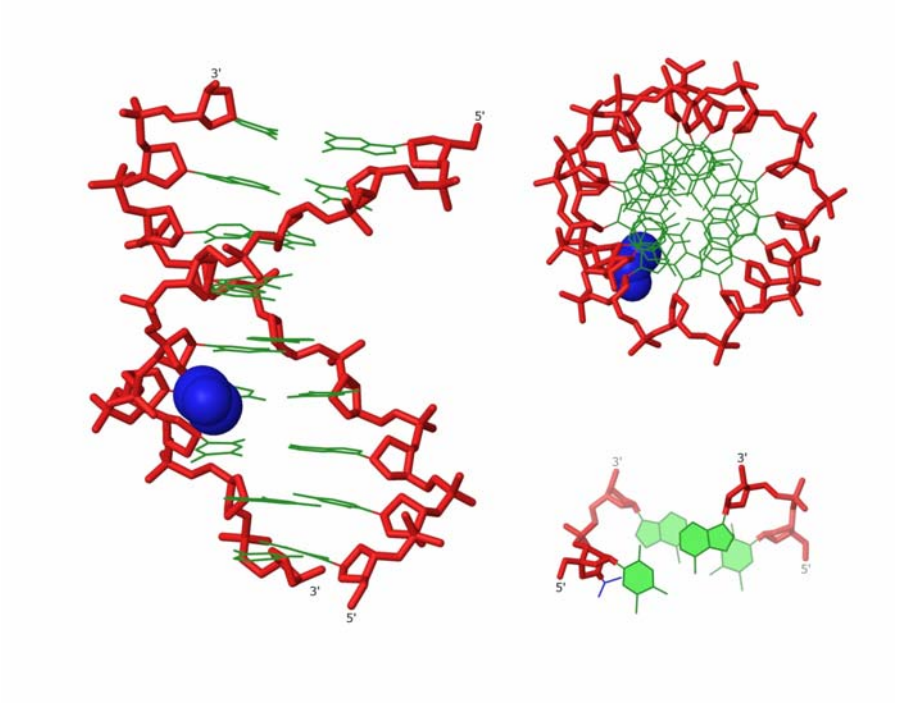

Figure S7. Three representations of the lowest energy structure of **V2**:**D2**, side view (left), top view (upper right) and truncated top view showing $\mathbf{V_5A_6}$:$\mathbf{T_{13}A_{14}}$ (lower right). For numbering of nucleotides see Fig. 4. Coloring scheme as in Fig. S3 except that the acetyl moiety of monomer **V** is in blue.

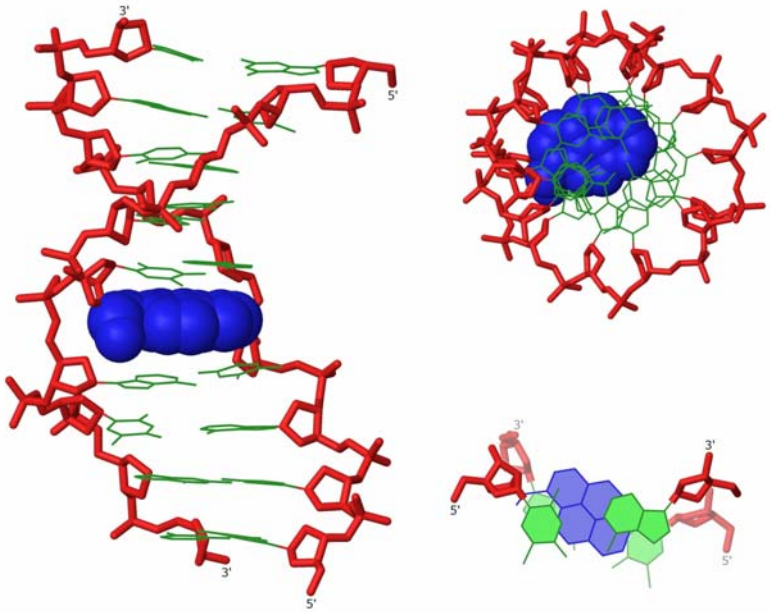

Figure S8. Three representations of the lowest energy structure of **X2**:**D2**, side view (left), top view (upper right) and truncated top view showing $\mathbf{X_5A_6}$:$\mathbf{T_{13}A_{14}}$ (lower right). For numbering of nucleotides see Fig. 4. Coloring scheme as in Fig. S3 except that the pyren-1-yl-carbonyl moiety of monomer **X** is in blue.

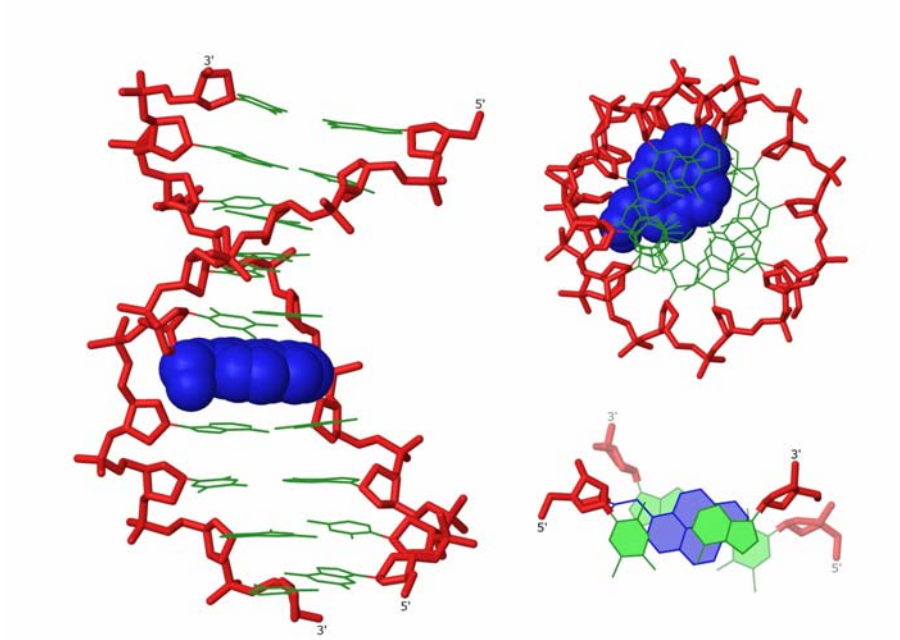

Figure S9. Three representations of the lowest energy structure of **Y2**:**D2**, side view (left), top view (upper right) and truncated top view showing $\mathbf{Y_5A_6}$:$\mathbf{T_{13}A_{14}}$ (lower right). For numbering of nucleotides see Fig. 4. Coloring scheme as in Fig. S3 except that the pyren-1-yl-acetyl moiety of monomer **Y** is in blue.

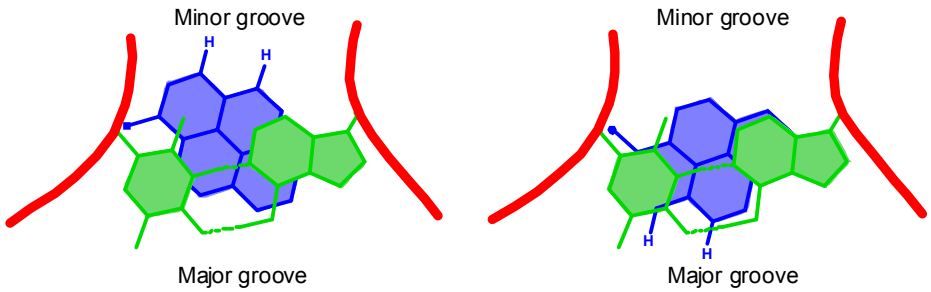

Figure S10. Top view of base pair (green) with an intercalated pyrene moiety (blue) illustrating the two major orientations of the pyrene moiety. H3 and H4 of pyrene have been included for clarity

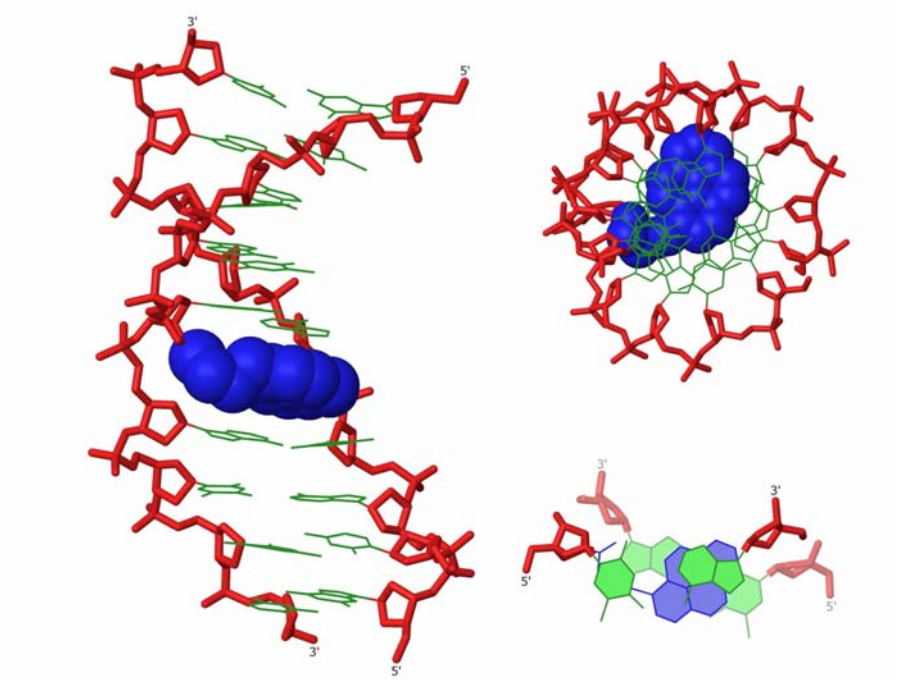

Figure S11. Three representations of the lowest energy structure of **Z2**:**D2** (intercalative binding mode), side view (left), top view (upper right) and truncated top view showing $\mathbf{Z_5A_6}$:$\mathbf{T_{13}A_{14}}$ (lower right). For numbering of nucleotides see Fig. 4. Coloring scheme as in Fig. S3 except that the 4-(pyren-1-yl)butanoyl moiety of monomer **Z** is in blue.

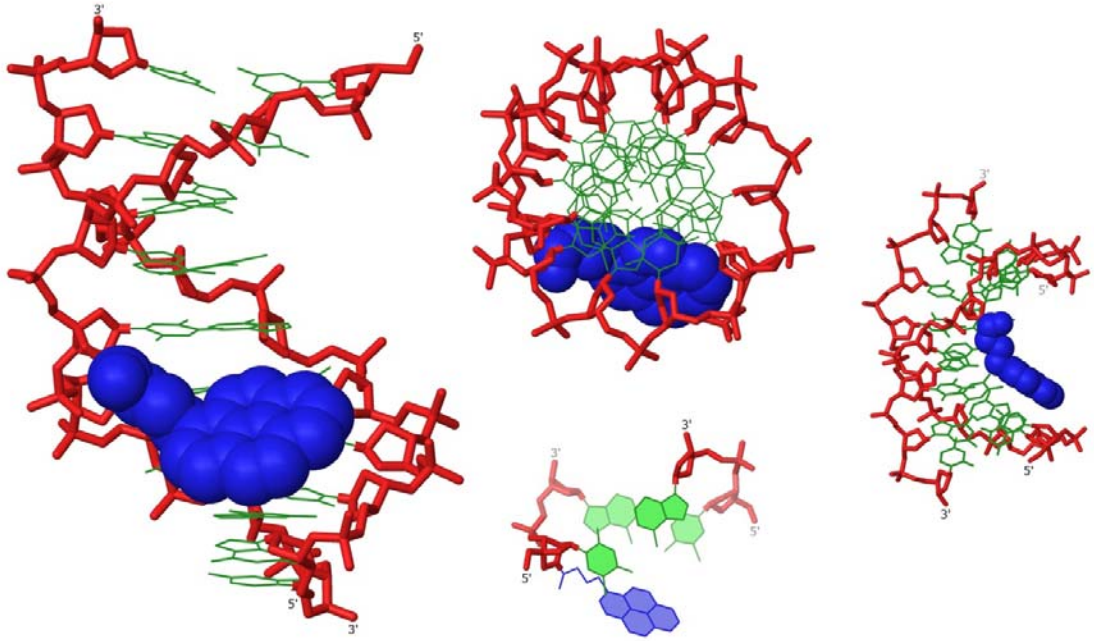

Figure S12. Four representations of the lowest energy structure of **Z2**:**D2** (non-intercalated binding mode), side view (left), top view (upper middle), truncated top view showing $\mathbf{Z_5A_6}$:$\mathbf{T_{13}A_{14}}$ (lower middle), and tilted view showing the position of the pyrene moiety in the major groove (right). For numbering of nucleotides see Fig. 4. Coloring scheme as in Fig. S3 except that the 4-(pyren-1-yl)butanoyl moiety of monomer **Z** is in blue.

Table S7. Pseudorotational phase angle *P* of nucleotides in the central region (**A**$_4$**B**$_5$**A**$_6$:**T**$_{13}$**A**$_{14}$**T**$_{15}$) of duplexes between **D1**, **O2**, **Q2**, **S2**, **V2**, **W2**, **X2**, **Y2** or **Z2** and complementary **D2**.[a]

	D1	O2	Q2	S2	V2	W2	X2	Y2	Z2[b]	Z2[c]
P(**A**$_4$)	114 [±29]	105 [±26]	121 [±23]	123 [±21]	124 [±22]	115 [±27]	111 [±36]	102 [±30]	81 [±30]	121 [±30]
P(**B**$_5$)	100 [±27]	17 [±5]	15 [±6]	9 [±5]	8 [±5]	15 [±5]	16 [±5]	16 [±5]	21 [±5]	7 [±5]
P(**A**$_6$)	112 [±22]	113 [±31]	97 [±21]	94 [±24]	149 [±27]	127 [±23]	109 [±21]	114 [±24]	95 [±26]	159 [±14]
P(**T**$_{13}$)	100 [±33]	81 [±26]	94 [±25]	97 [±26]	108 [±27]	92 [±28]	98 [±29]	76 [±22]	86 [±22]	113 [±22]
P(**A**$_{14}$)	117 [±23]	113 [±21]	106 [±26]	103 [±22]	94 [±20]	123 [±38]	108 [±31]	105 [±27]	104 [±26]	94 [±22]
P(**T**$_{15}$)	103 [±23]	94 [±20]	98 [±24]	102 [±24]	102 [±27]	96 [±24]	98 [±22]	103 [±26]	101 [±24]	115 [±22]

[a] Pseudorotational phase angle *P* given as mean [± standard deviation]. For nucleotide numbering for the duplexes studied by molecular modeling – see Fig. 4 in main manuscript.

[b] Values for **Z2**:**D2** with pyrene in intercalated position.

[c] Values for **Z2**:**D2** with pyrene in major groove position.

Table S8. Glycosidic torsion angle χ of nucleotides in the central region (**A**$_4$**B**$_5$**A**$_6$:**T**$_{13}$**A**$_{14}$**T**$_{15}$) of duplexes between **D1**, **O2**, **Q2**, **S2**, **V2**, **W2**, **X2**, **Y2** or **Z2** and complementary **D2**.[a]

	D1	O2	Q2	S2	V2	W2	X2	Y2	Z2[b]	Z2[c]
χ(**A**$_4$)	-144 [±17]	-139 [±16]	-128 [±15]	-130 [±16]	-137 [±15]	-129 [±18]	-133 [±21]	-139 [±19]	-148 [±15]	-140 [±16]
χ(**B**$_5$)	-143 [±15]	-175 [±8]	-168 [±8]	-159 [±8]	-157 [±9]	-174 [±8]	-169 [±7]	-171 [±7]	-175 [±7]	-153 [±8]
χ(**A**$_6$)	-134 [±15]	-143 [±18]	-147 [±14]	-151 [±15]	-130 [±15]	-105 [±16]	-113 [±23]	-115 [±21]	-150 [±15]	-115 [±11]
χ(**T**$_{13}$)	-146 [±15]	-140 [±13]	-141 [±12]	-137 [±14]	-137 [±16]	-134 [±14]	-134 [±13]	-130 [±11]	-133 [±12]	-132 [±13]
χ(**A**$_{14}$)	-131 [±15]	-135 [±14]	-142 [±16]	-143 [±14]	-144 [±12]	-134 [±20]	-147 [±20]	-148 [±14]	-153 [±14]	-137 [±12]
χ(**T**$_{15}$)	-137 [±14]	-146 [±12]	-142 [±13]	-138 [±13]	-137 [±14]	-149 [±13]	-144 [±12]	-147 [±16]	-146 [±13]	-115 [±25]

[a] Glycosidic torsion angle χ given as mean [± standard deviation]. For nucleotide numbering for the duplexes studied by molecular modeling – see Fig. 4 in main manuscript.

[b] Values for **Z2**:**D2** with pyrene in intercalated position.

[c] Values for **Z2**:**D2** with pyrene in major groove position.

References

‖A research center funded by the Danish National Research Foundation for studies on nucleic acid chemical biology.

S1) Gottlieb, H. E.; Kotlyar, V.; Nudelman, A. *J. Org. Chem.* **1997**, *62*, 7512-7515.

S2) Kumar, T. S.; Madsen, A. S.; Wengel, J.; Hrdlicka, P. J. *J. Org. Chem.* **2006**, *71*, 4188-4201.

S3) Assignments of ^{1}H NMR signals of H-5′ and H-5″ (and of the corresponding ^{13}C signals) may in principle be interchanged.

S4) The integral of the H-1′-signal of the least predominant rotamer (termed B) is set to 1.0.

S5) Hrdlicka, P. J.; Kumar, T. S.; Wengel, J. *Chem. Commun.* **2005**, 4279-4281.

S6) Kumar, T. S.; Wengel, J.; Hrdlicka, P. J. *ChemBioChem*. **2007**, *8*, 1122-1125.

S7) Kumar, T. S.; Madsen, A. S.; Østergaard, M. E.; Wengel, J.; Hrdlicka, P. J. *J. Org. Chem.* **2008**, *73*, 7060-7066.

S8) Yamana, K.; Iwase, R.; Furutani, S.; Tsuchida, H.; Zako, H.; Yamaoka, T.; Murakami, A. *Nucleic Acids Res.* **1999**, *27*, 2387-2392.

S9) Nakamura, M.; Fukunaga, Y.; Sasa, K.; Ohtoshi, Y.; Kanaori, K.; Hayashi, H.; Nakano, H.; Yamana, K. *Nucleic Acids Res.* **2005**, *33*, 5887-5895.

S10) MacroModel version 9.1, S., LLC, New York, NY, **2005**.

S11) a) Weiner, S. J.; Kollman, P. A.; Case, D. A.; Singh, U. C.; Ghio, C.; Alagona, G.; Profeta, S.; Weiner, P. *J. Am. Chem. Soc.* **1984**, *106*, 765-784, b) Weiner, S. J.; Kollman, P. A.; Nguyen, D. T.; Case, D. A. *J. Comp. Chem.* **1986**, *7*, 230-252.

S12) Still, W. C.; Tempczyk, A.; Hawley, R. C.; Hendrickson, T. *J. Am. Chem. Soc.* **1990**, *112*, 6127-6129.

S13) Nielsen, K. M. E.; Petersen, M.; Håkansson, A. E.; Wengel, J.; Jacobsen, J. P. *Chem. Eur. J.* **2002**, *8*, 3001-3009.

S14) Rodger, A.; Norden, B. *Circular Dichroism & Linear Dichoism*, Oxford University Press, NY, 1997.

S15) Petersen, M.; Håkansson, A. E.; Wengel, J.; Jacobsen, J. P. *J. Am. Chem. Soc.* **2001**, *123*, 7431-7432.

S16) The furanose ring of α-L-LNA is, according to definitions, conformationally restricted in an N-type conformation as a result of the L-configuration; however, α-L-LNA does not overlay onto a typical *N*-type framework but rather overlays an *S*-type framework.

S17) Schneider, B.; Neidle, S.; Berman, H. M. *Biopolymers* **1997**, *42*, 113-124.

S18) Rajwanshi, V. K.; Håkansson, A. E.; Sørensen, M. D.; Pitsch, S.; Singh, S. K.; Kumar, R.; Nielsen, P.; Wengel, J. *Angew. Chem. Int. Ed.* **2000**, *39*, 1656-1659.

S19) Narlikar, G. J.; Khosla, M.; Usman, N.; Herschlag, D. *Biochemistry* **1997**, *36*, 2465-2477.

S20) Gherghe, C. M.; Krahn, J. M.; Weeks, K. M. *J. Am. Chem. Soc.* **2005**, *127*, 13622-13628.

S21) Honcharenko, D.; Vargese, O. P.; Plashkevych, O.; Barman, J.; Chattopadhyaya, J. *J. Org. Chem.* **2006**, *71*, 299-314.

S22) Egli, M.; Tereshko, V.; Teplova, M.; Minasov, G.; Joachimiak, A.; Sanishvili, R.; Weeks, C. M.; Miller, R.; Maier, M. A.; An, H.; Cook, P. D., Manoharan, M. *Biopolymers* **1998**, *48*, 234-252.

S23) Kielkopf, C. L.; Ding, S.; Kuhn, P.; Rees, D. C. *J. Mol. Biol.* **2000**, *296*, 787-801.

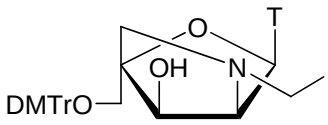

2S

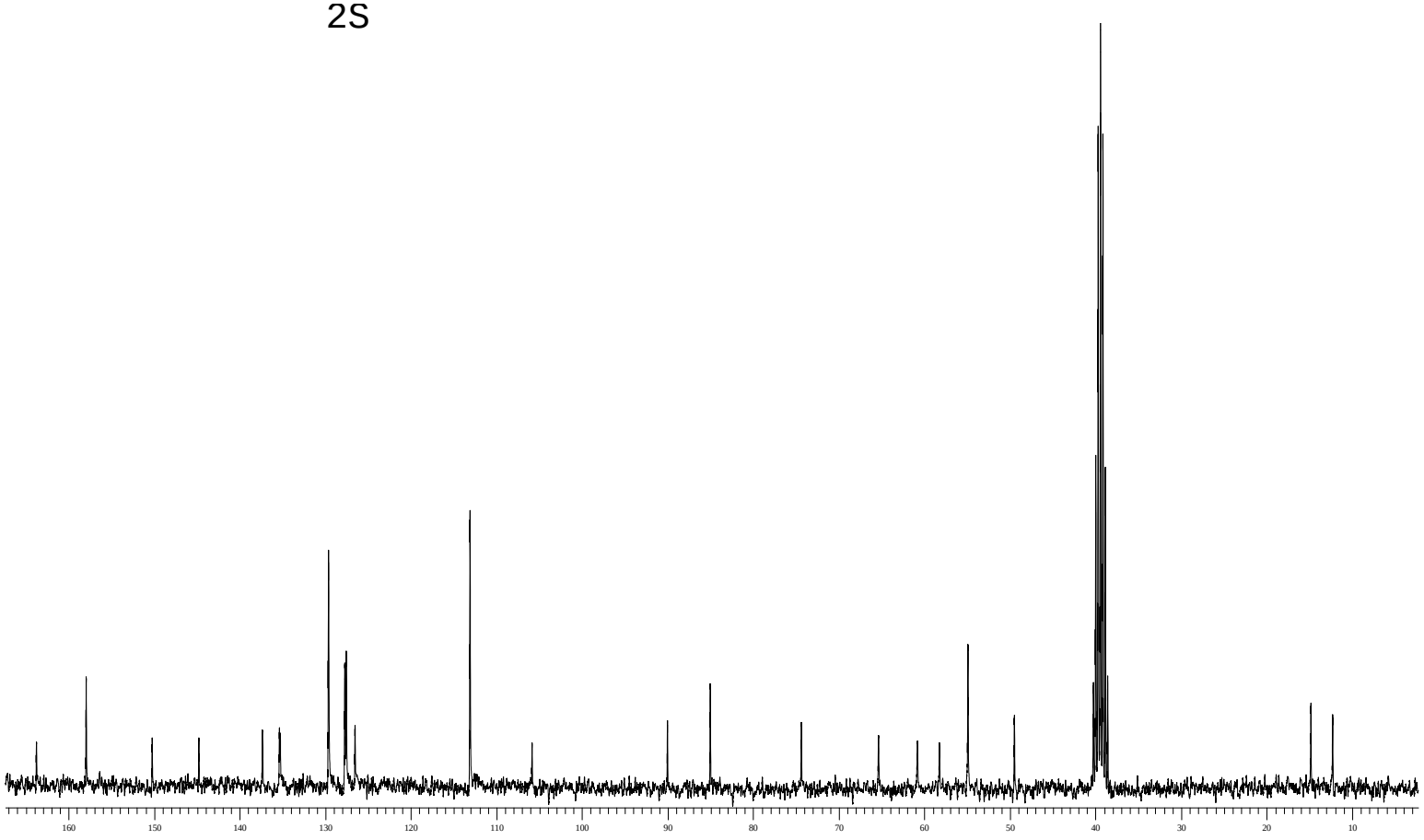

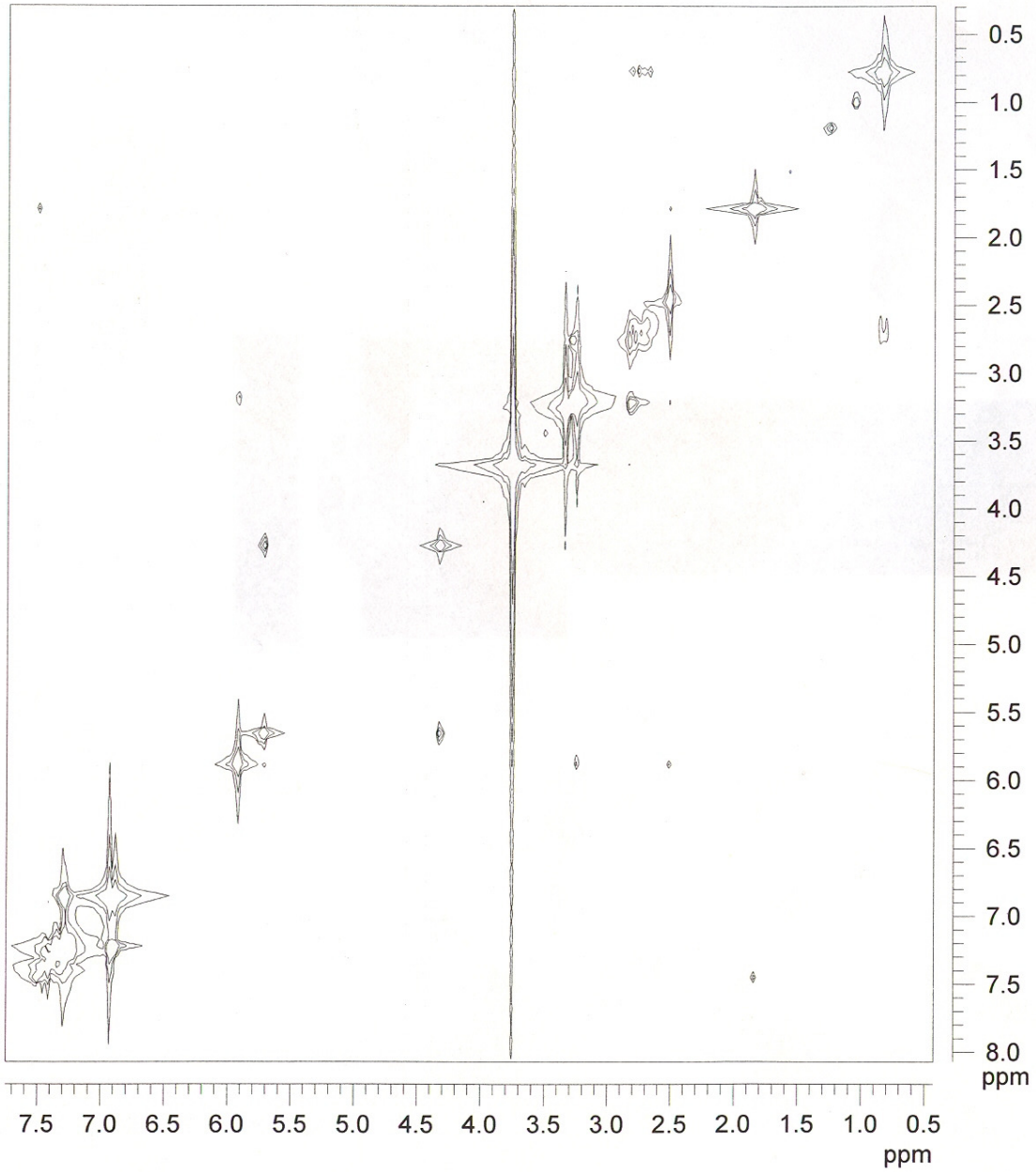
0.5
1.0
1.5
2.0
2.5
3.0
3.5
4.0
4.5
5.0
5.5
6.0
6.5
7.0
7.5
8.0
ppm
7.5 7.0 6.5 6.0 5.5 5.0 4.5 4.0 3.5 3.0 2.5 2.0 1.5 1.0 0.5
ppm

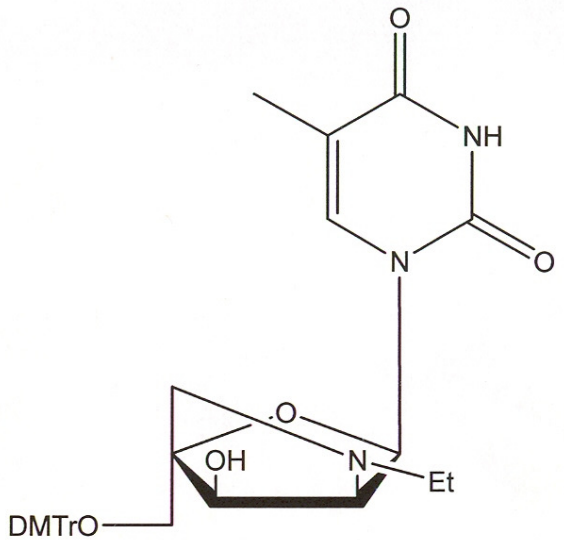
O
NH
N
O
O
OH
N
Et
DMTrO

2S

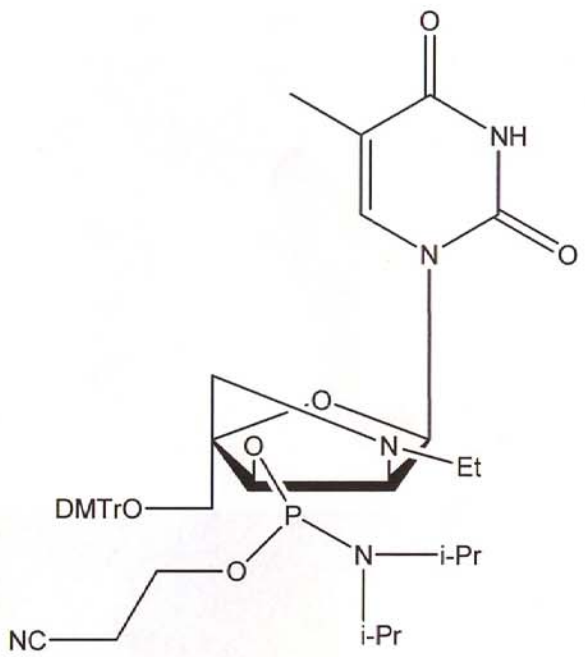

3S

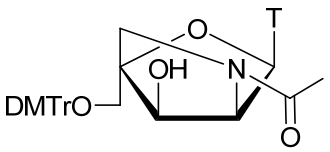
O
T
OH
N
DMTrO
O

2V

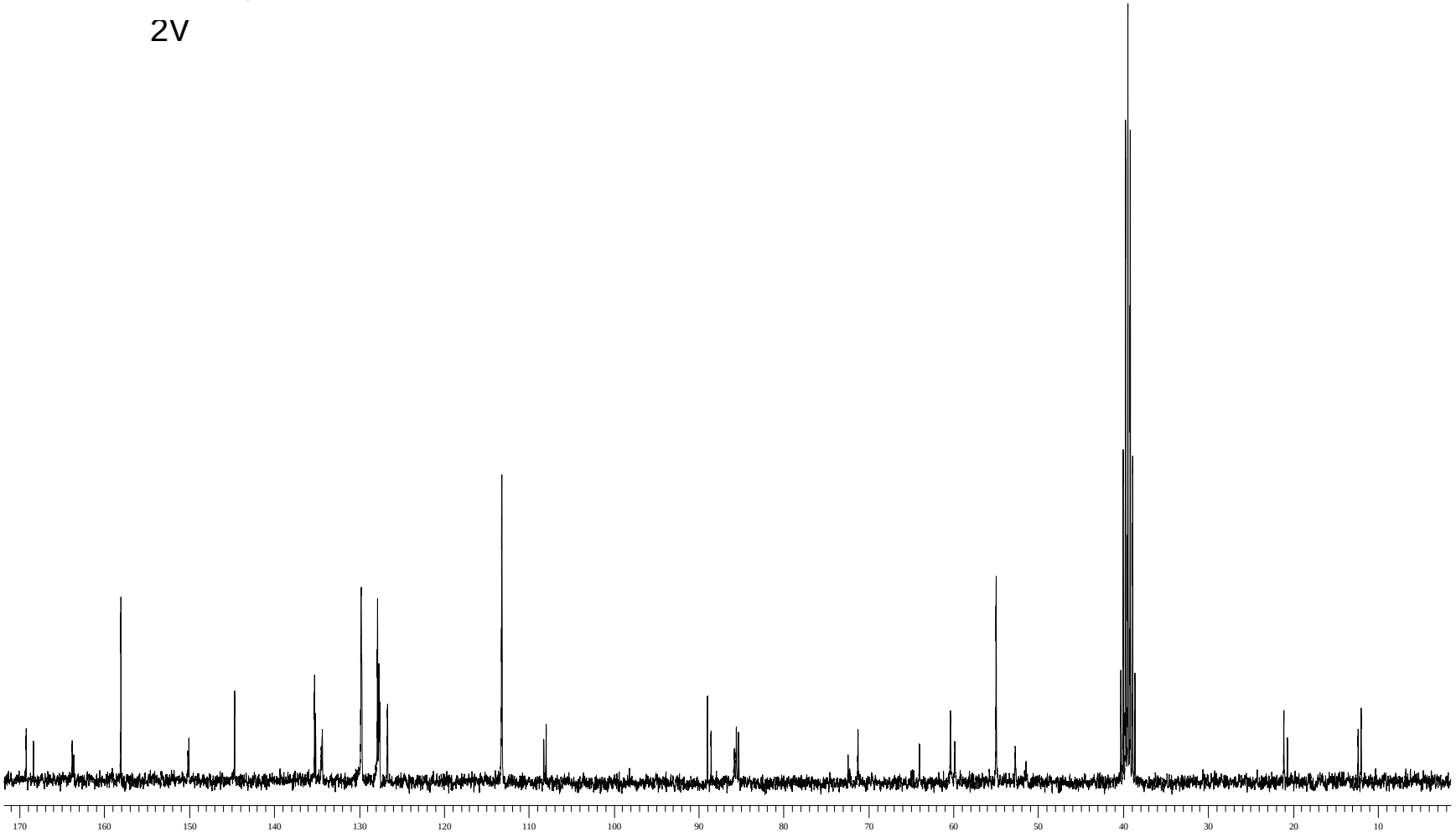
170
160
150
140
130
120
110
100
90
80
70
60
50
40
30
20
10

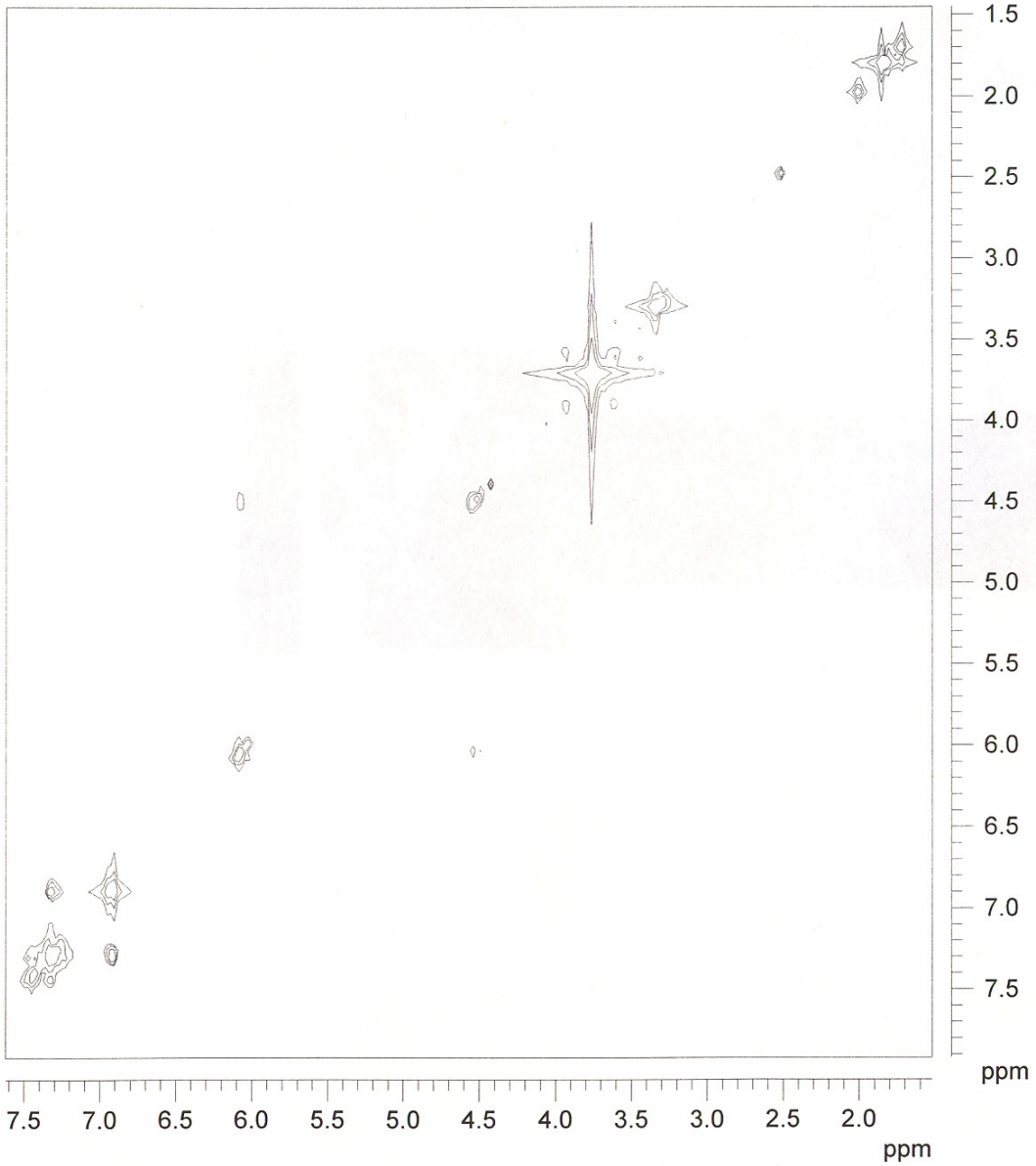
1.5
2.0
2.5
3.0
3.5
4.0
4.5
5.0
5.5
6.0
6.5
7.0
7.5
ppm
7.5 7.0 6.5 6.0 5.5 5.0 4.5 4.0 3.5 3.0 2.5 2.0
ppm

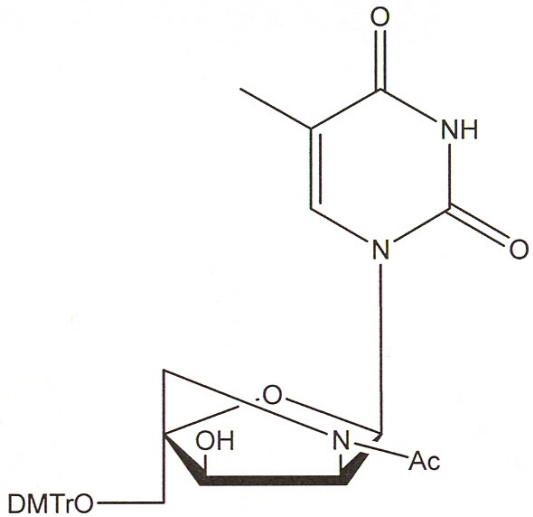
O
NH
N
O
O
OH
N
Ac
DMTrO

2V

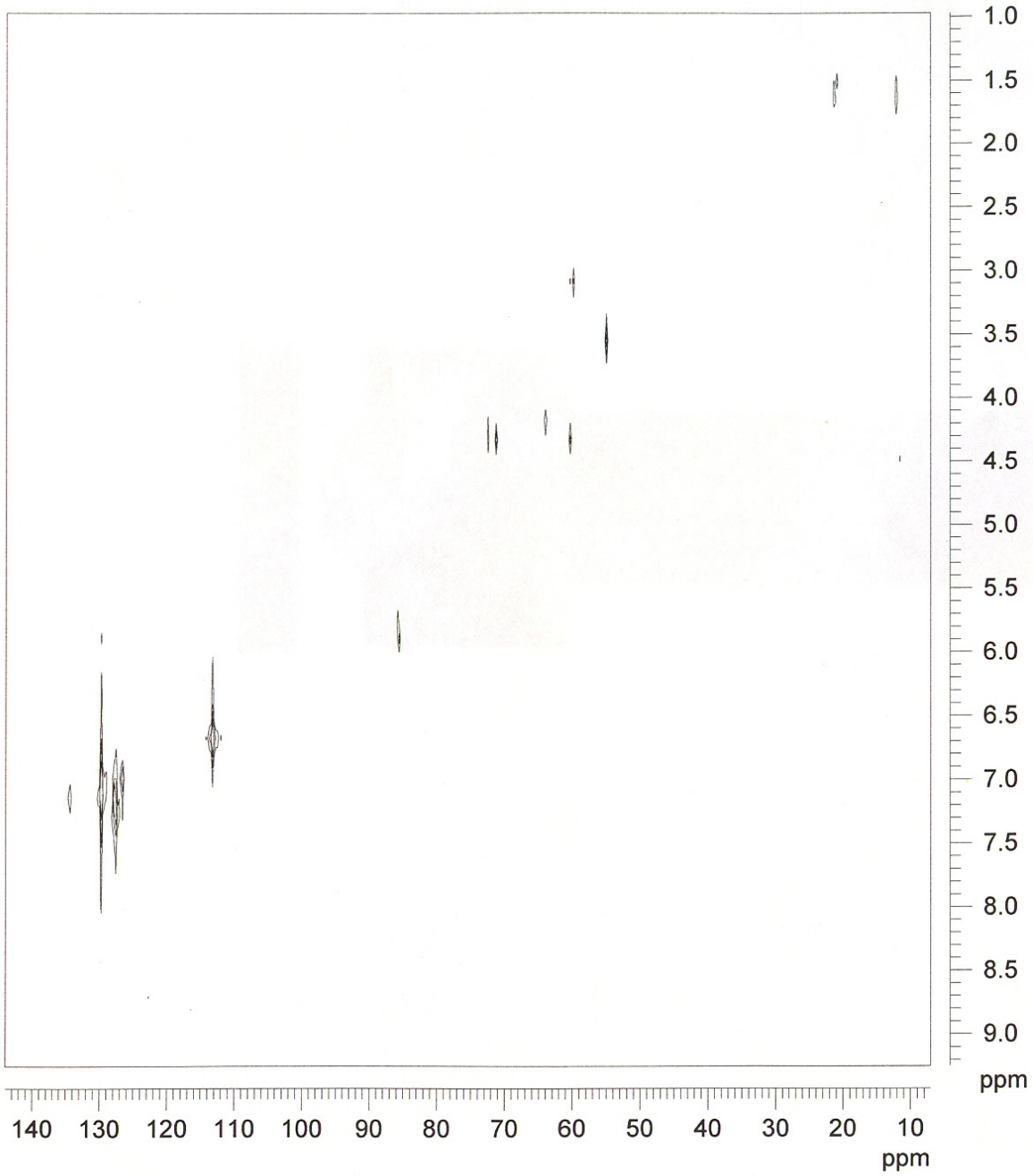
1.0
1.5
2.0
2.5
3.0
3.5
4.0
4.5
5.0
5.5
6.0
6.5
7.0
7.5
8.0
8.5
9.0
ppm
140 130 120 110 100 90 80 70 60 50 40 30 20 10
ppm

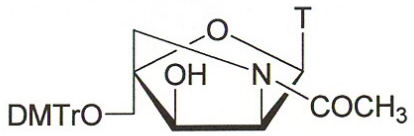
O
T
OH
N
DMTrO
COCH3

2V

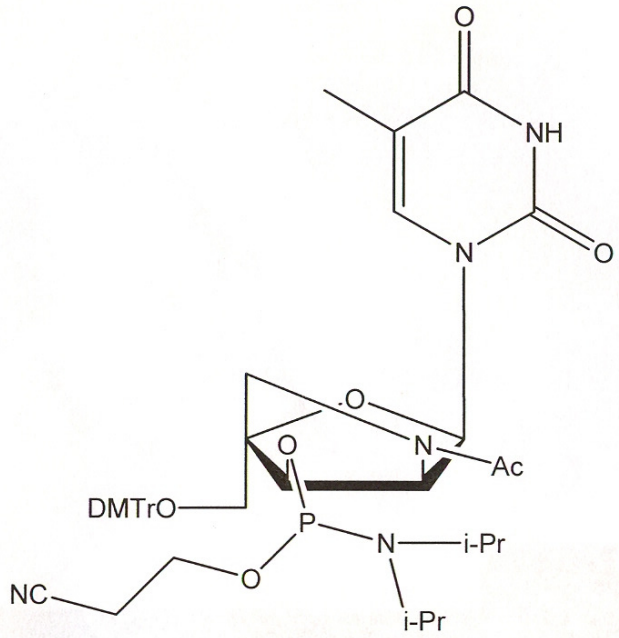

3V

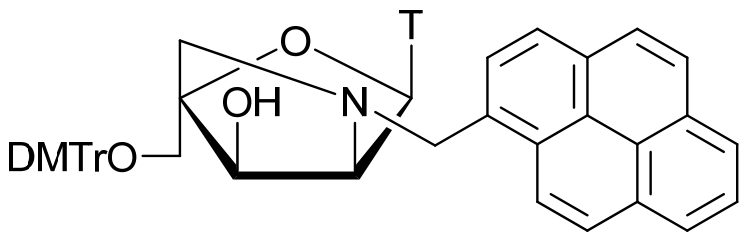
O
T
OH
N
DMTrO

2W

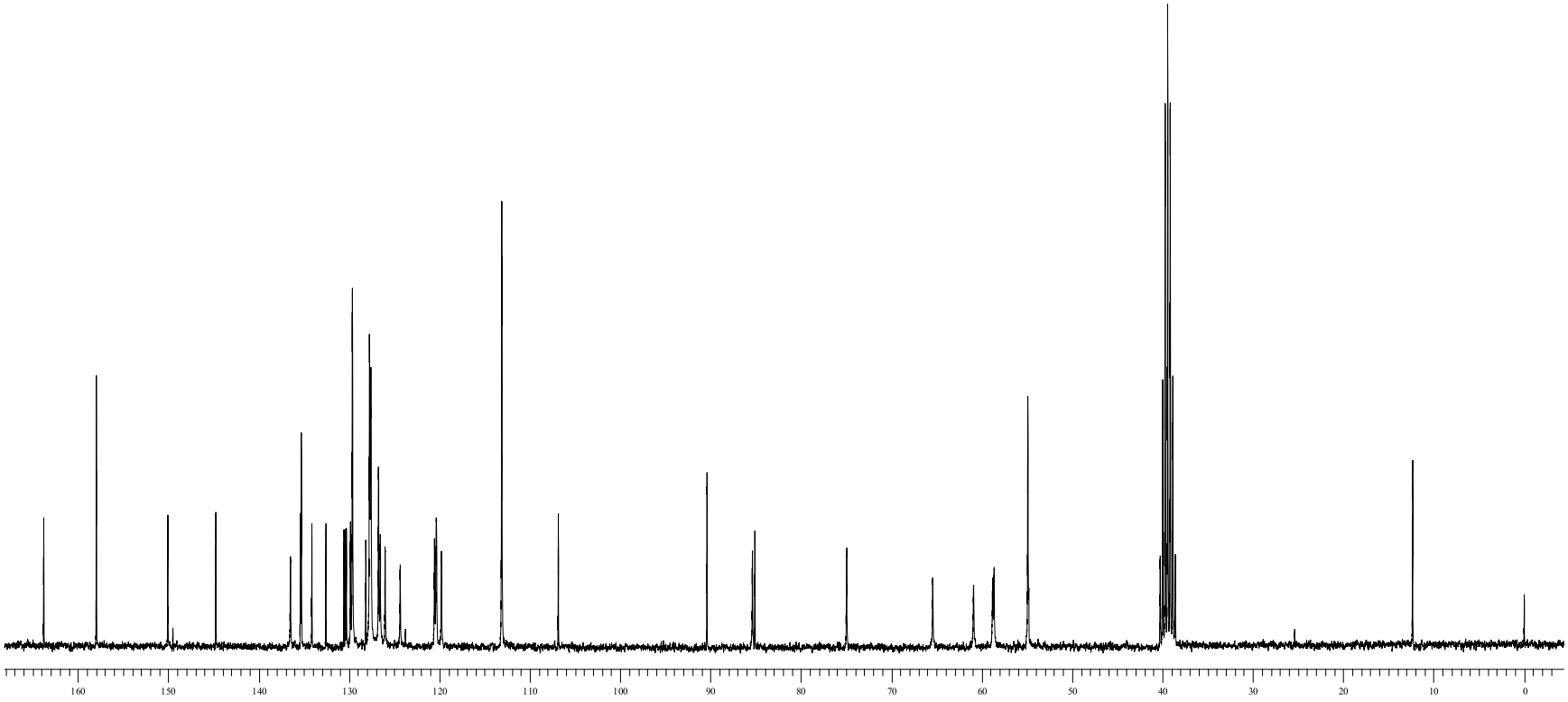
160
150
140
130
120
110
100
90
80
70
60
50
40
30
20
10
0

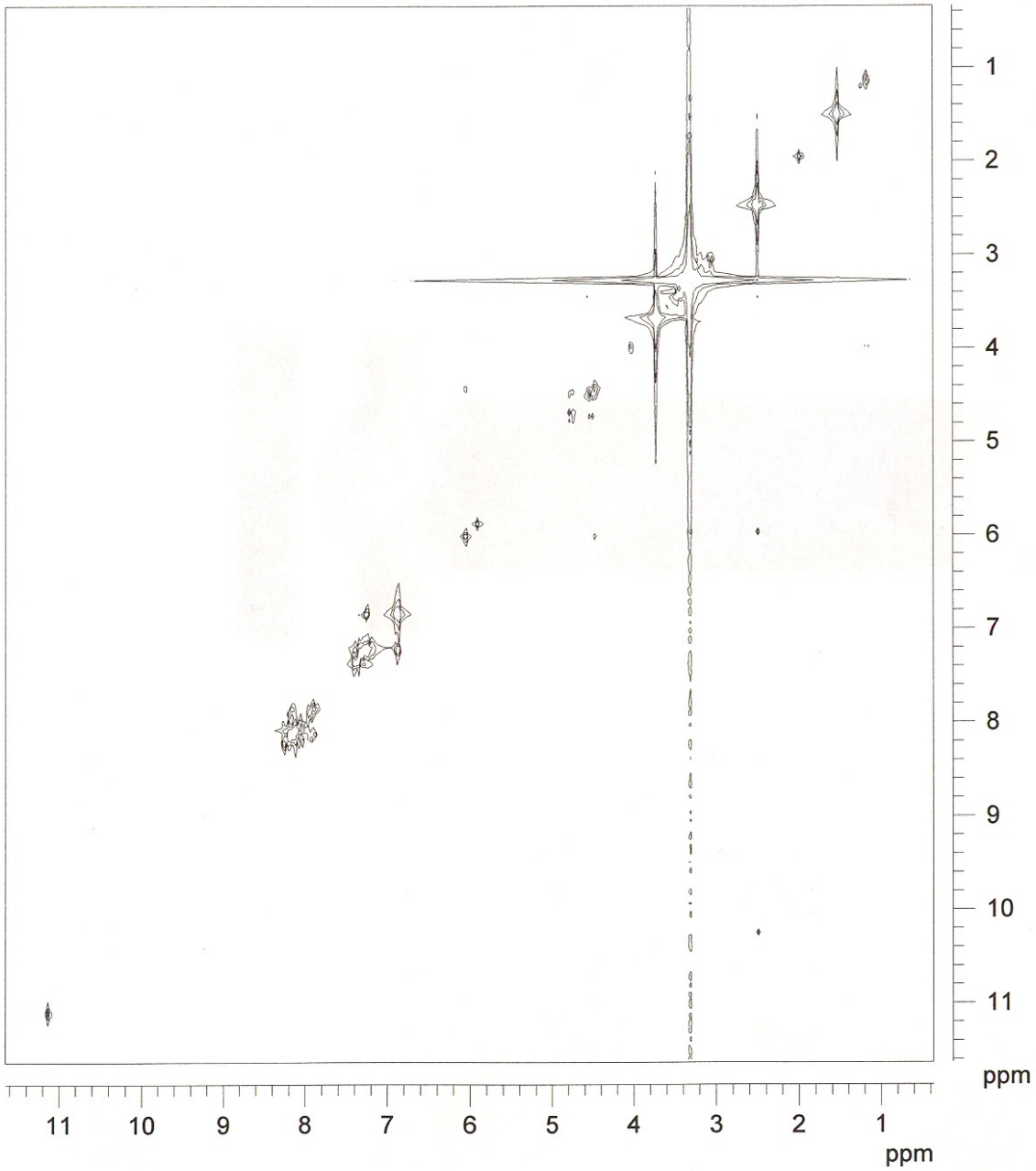

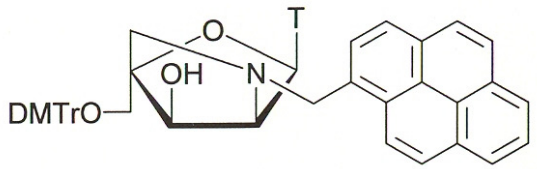

2W

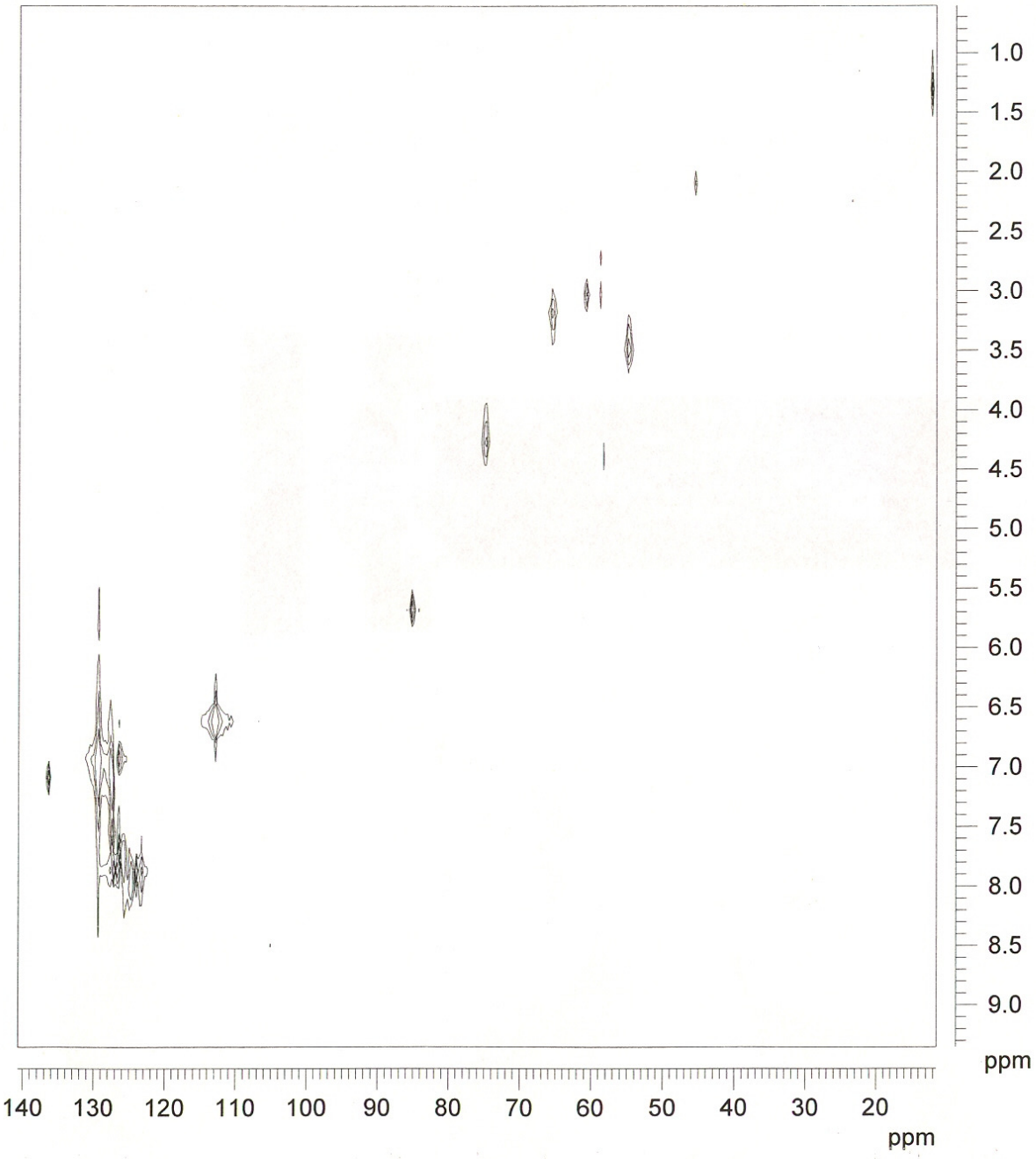
1.0
1.5
2.0
2.5
3.0
3.5
4.0
4.5
5.0
5.5
6.0
6.5
7.0
7.5
8.0
8.5
9.0
ppm
140
130
120
110
100
90
80
70
60
50
40
30
20
ppm

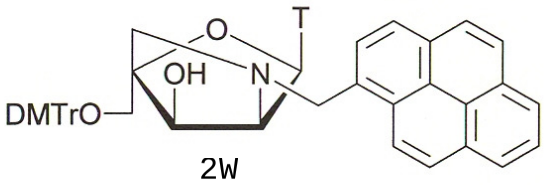
O
T
OH
N
DMTrO

2W

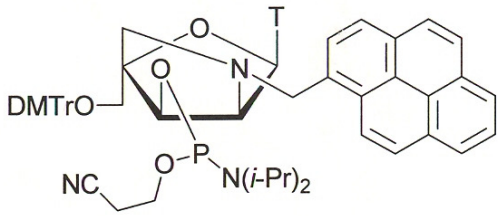

3W

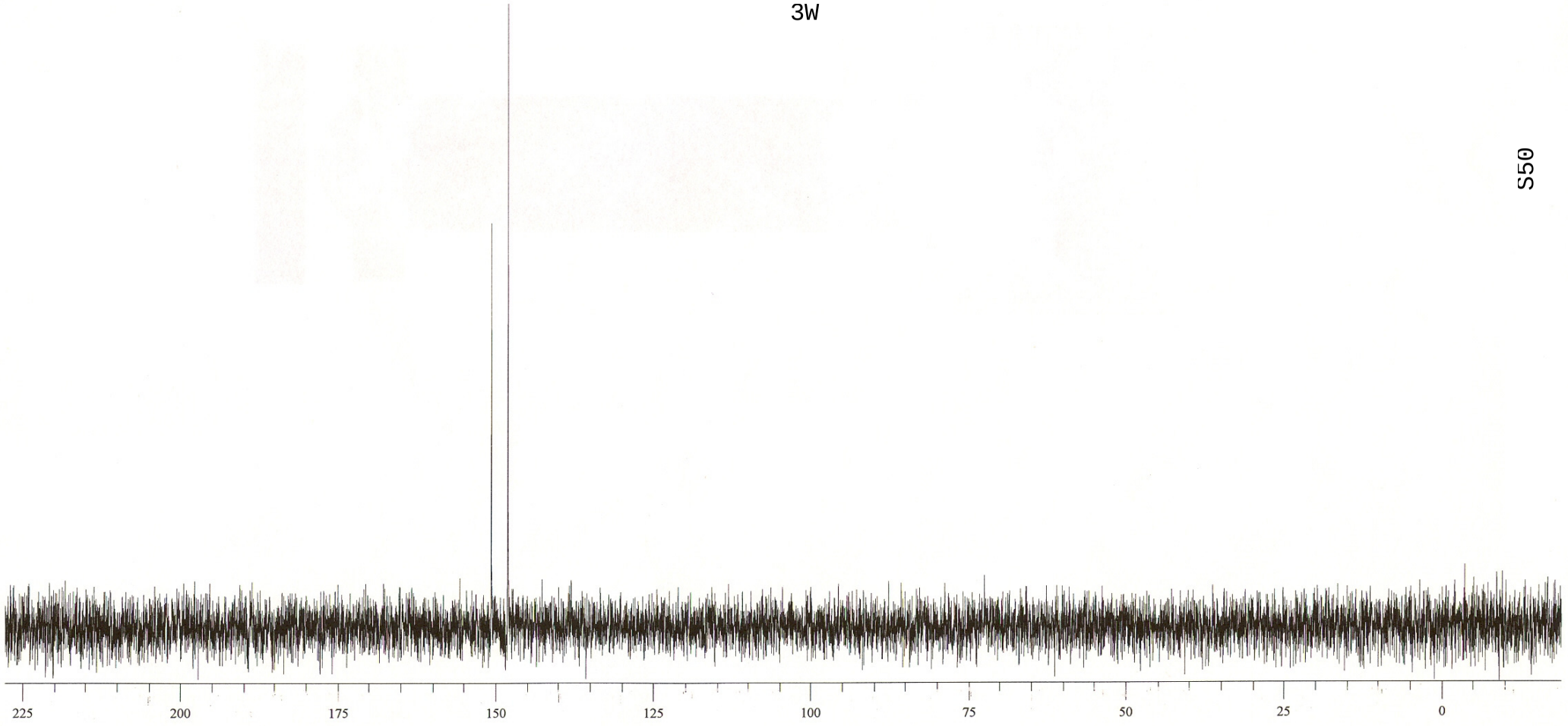

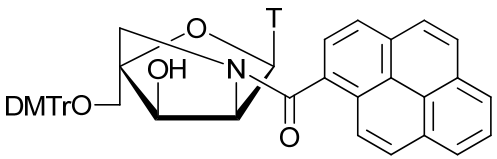
O
T
OH
N
DMTrO
O

2X

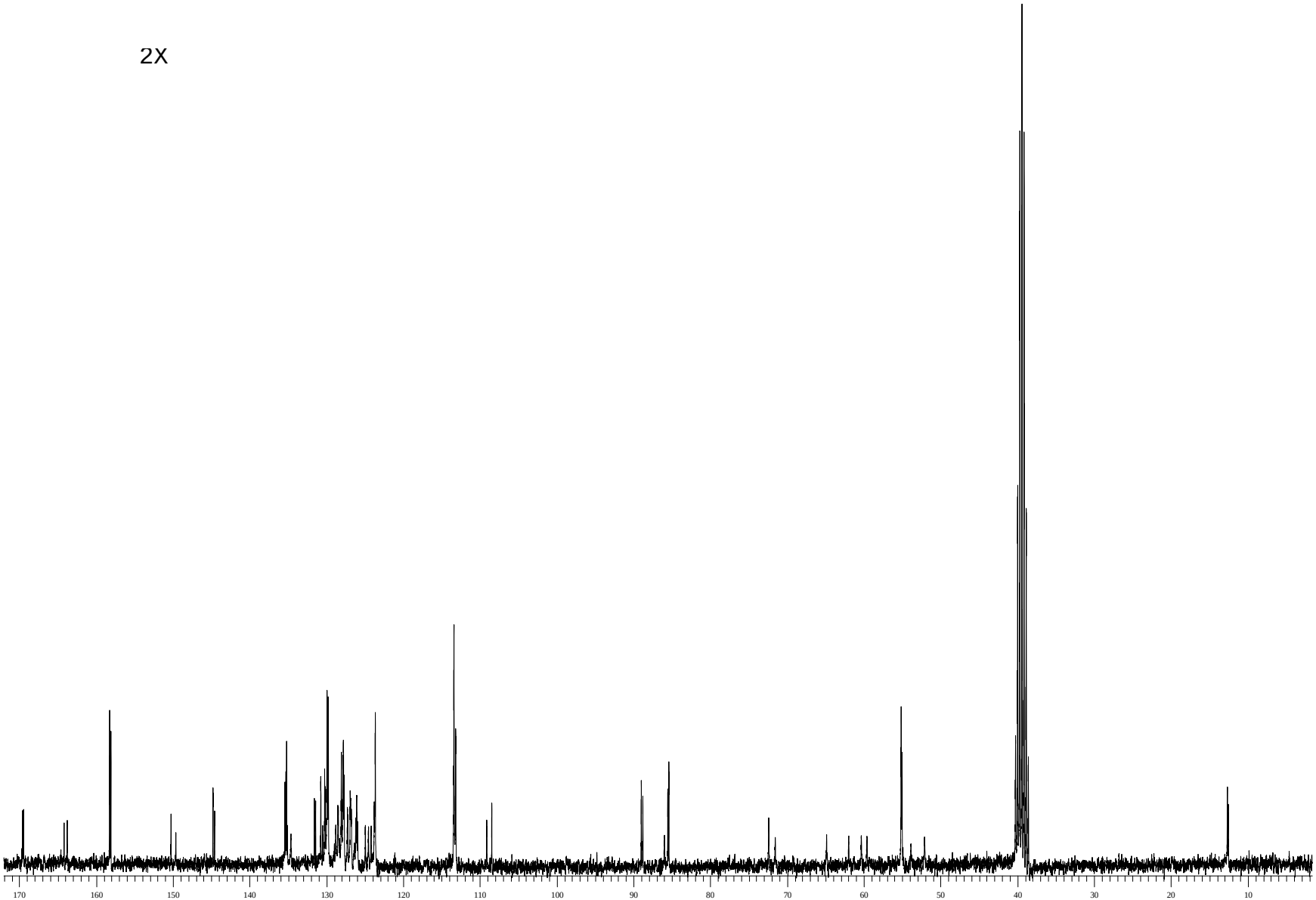
170
160
150
140
130
120
110
100
90
80
70
60
50
40
30
20
10

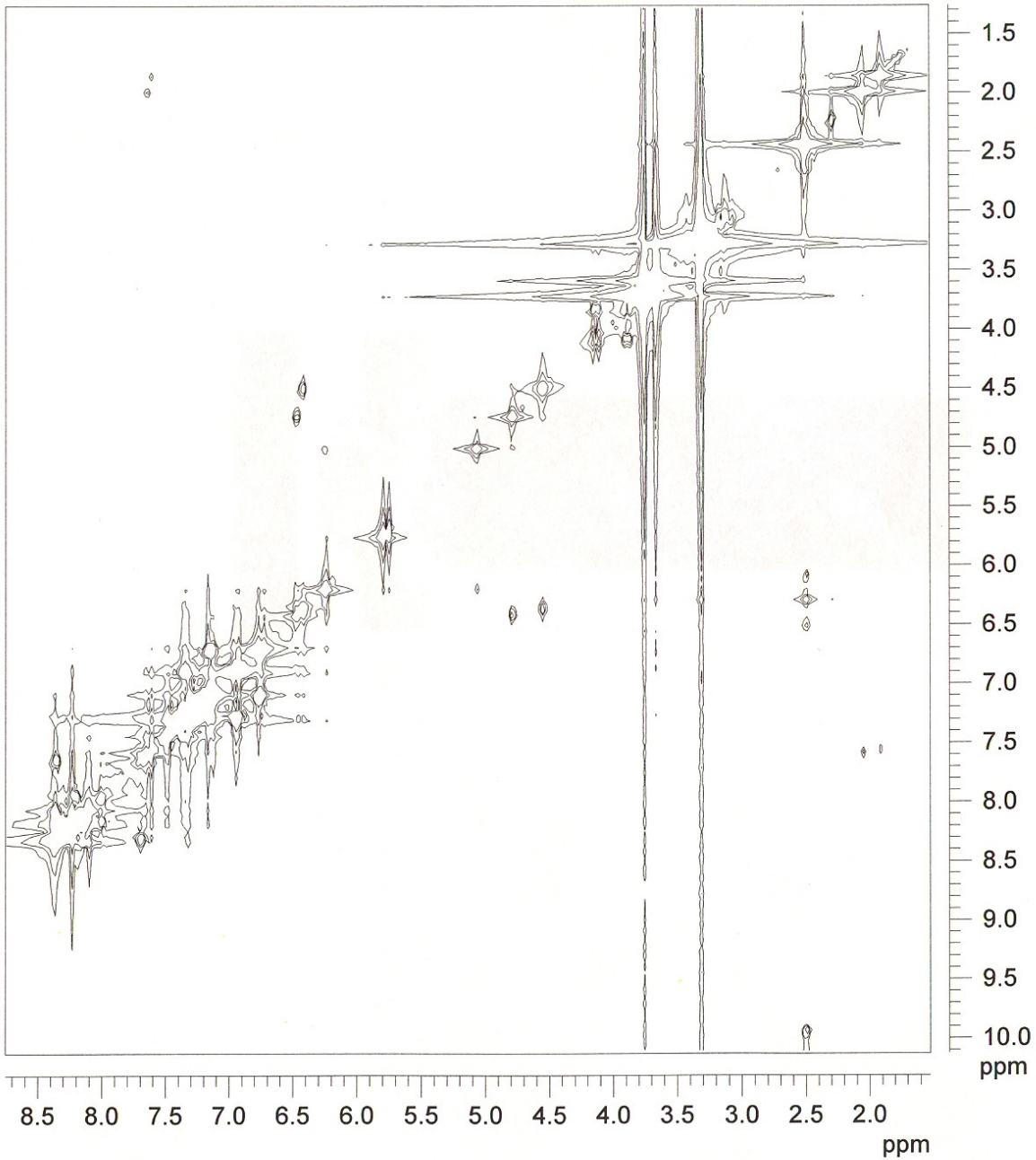
1.5
2.0
2.5
3.0
3.5
4.0
4.5
5.0
5.5
6.0
6.5
7.0
7.5
8.0
8.5
9.0
9.5
10.0
ppm
8.5 8.0 7.5 7.0 6.5 6.0 5.5 5.0 4.5 4.0 3.5 3.0 2.5 2.0
ppm

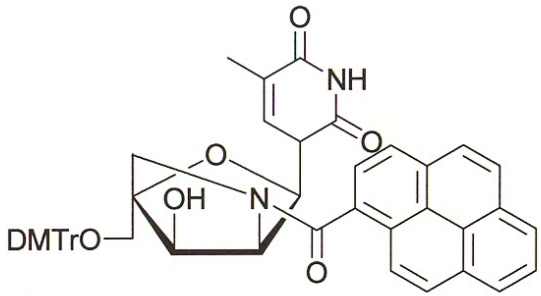
O
NH
O
O
OH
N
DMTrO
O

2X

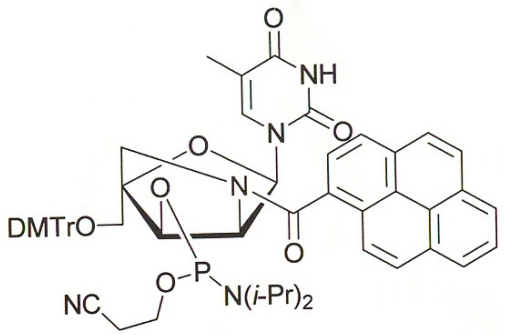

3X

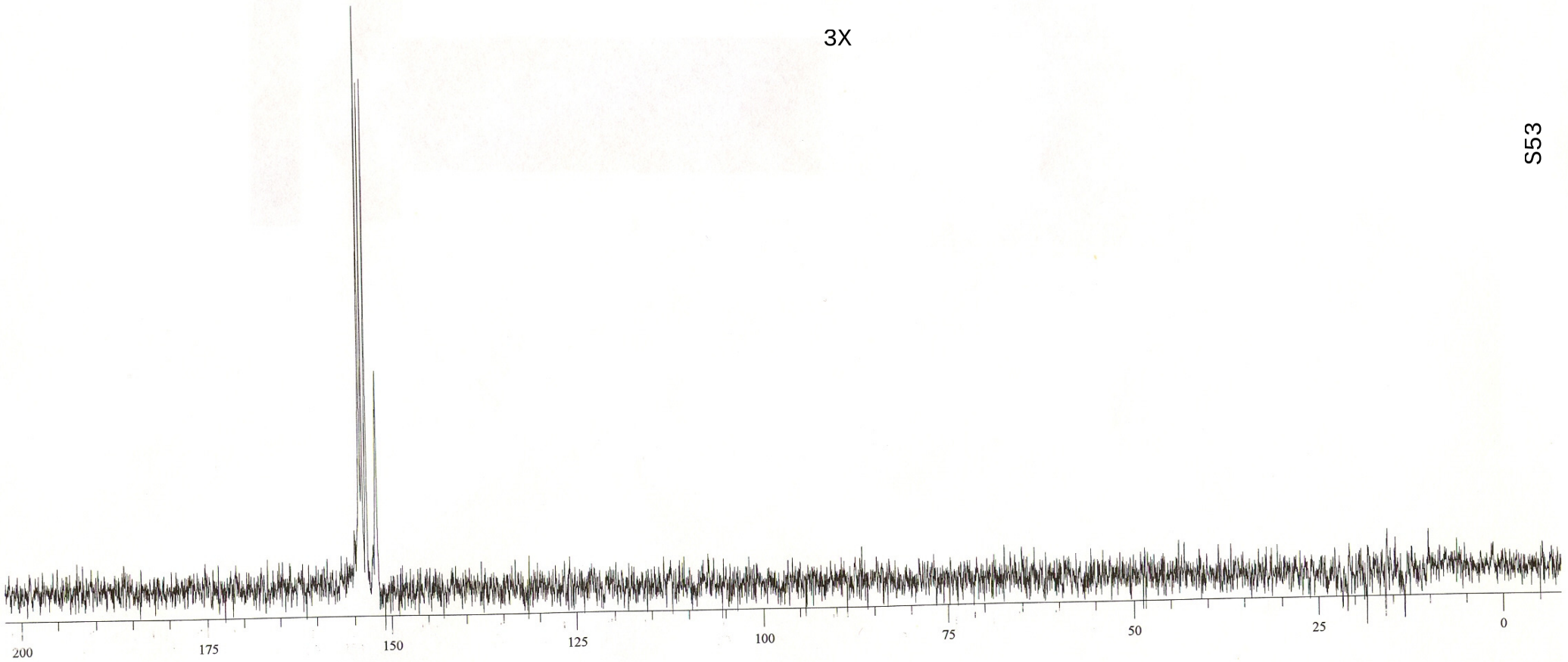

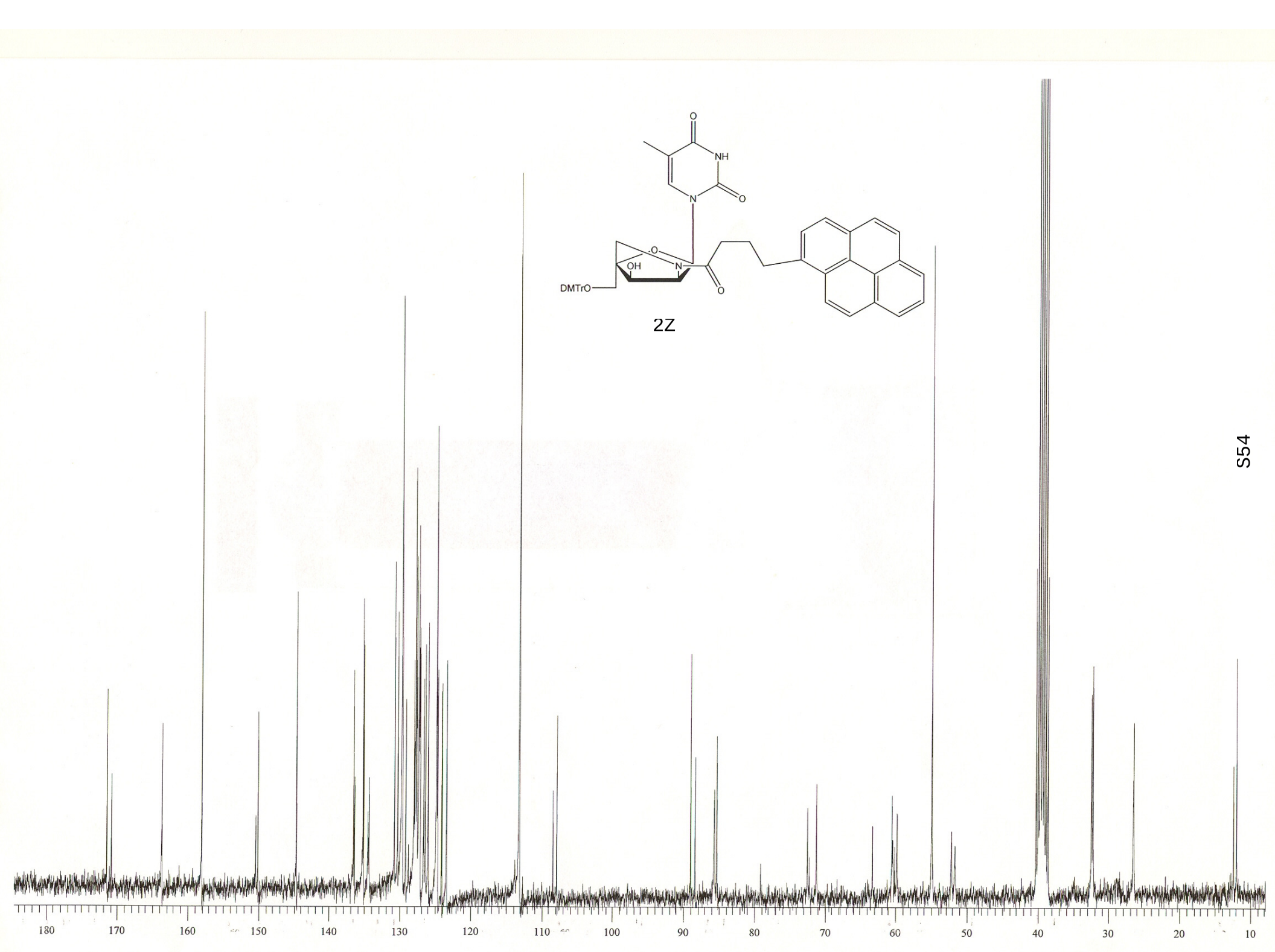
O
NH
N
O
O
OH
N
DMTrO
O
2Z
180
170
160
150
140
130
120
110
100
90
80
70
60
50
40
30
20
10

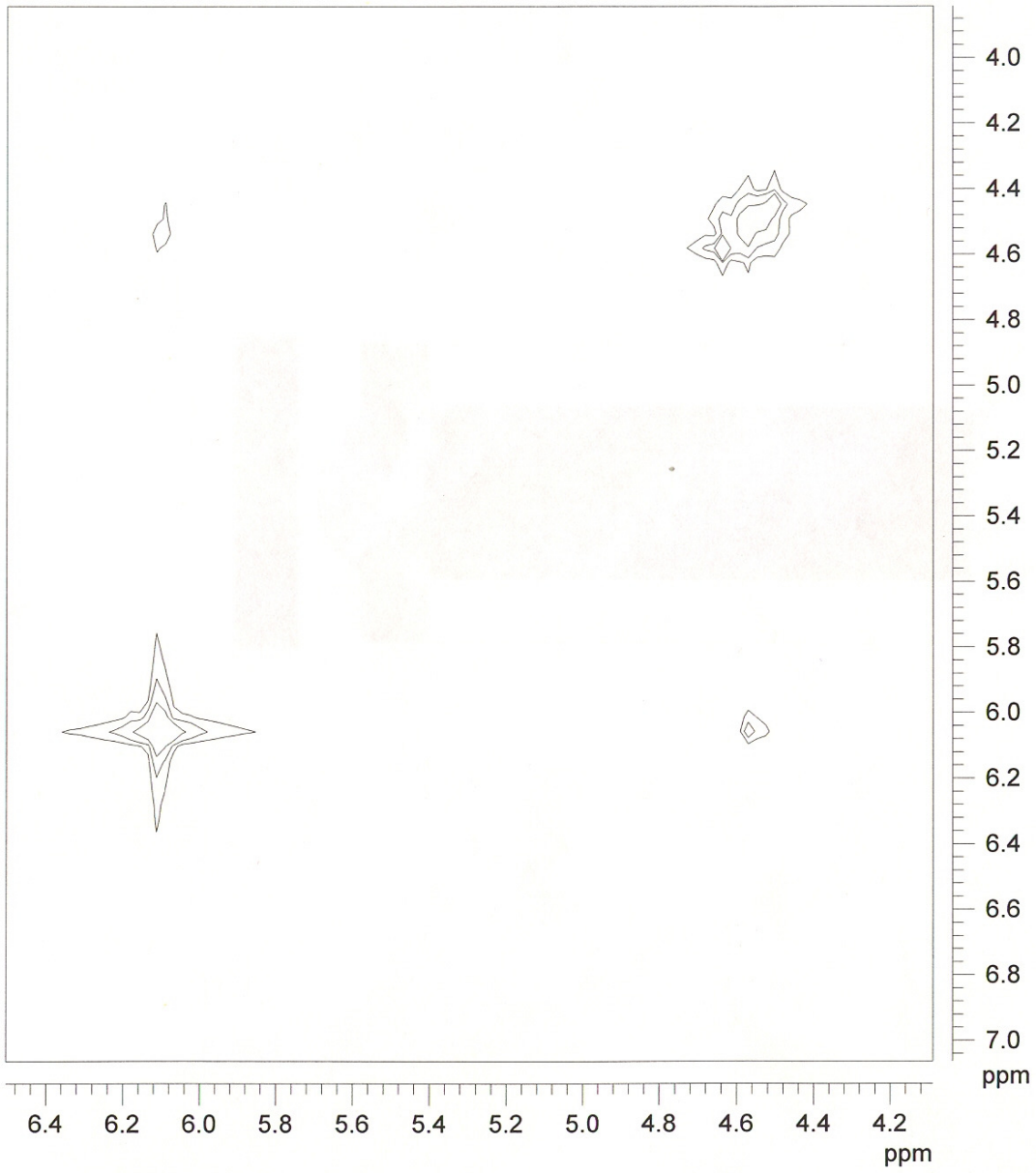
4.0
4.2
4.4
4.6
4.8
5.0
5.2
5.4
5.6
5.8
6.0
6.2
6.4
6.6
6.8
7.0
ppm
6.4
6.2
6.0
5.8
5.6
5.4
5.2
5.0
4.8
4.6
4.4
4.2
ppm

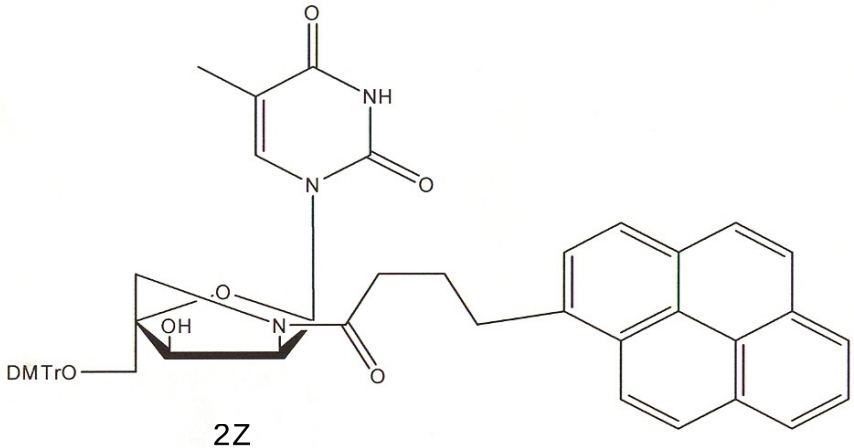
O
NH
N
O
O
OH
N
O
DMTrO

2Z

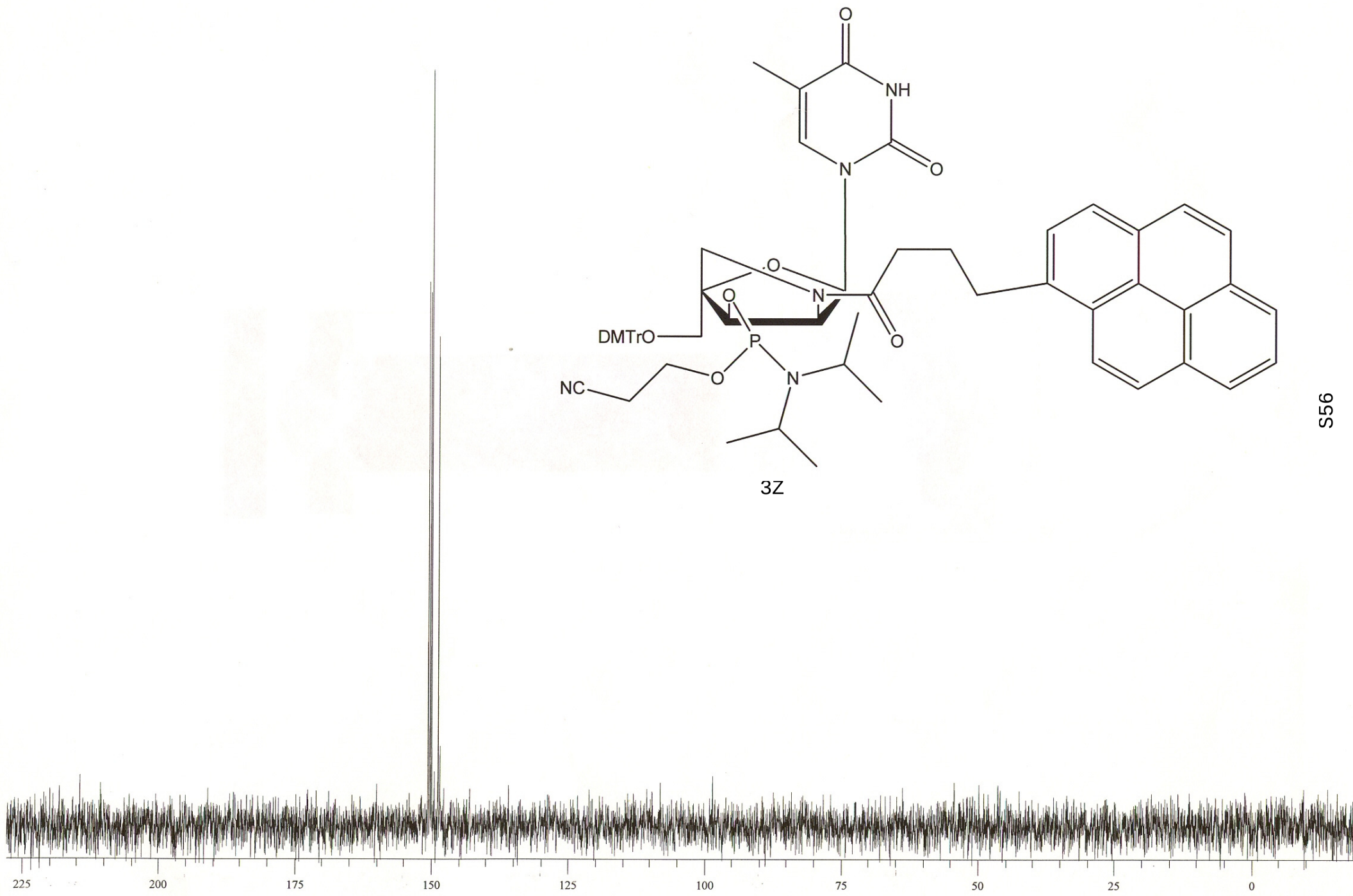

3Z